Mathematical Biosciences and Engineering

https://www.aimspress.com/journal/mbe

MBE, 23(1): 210–241.
DOI: 10.3934/mbe.2026009
Received: 16 August 2025
Revised: 29 October 2025
Accepted: 17 November 2025
Published: 04 December 2025

Research article

Nonlinear bioheat model for dynamics of hypothermia and frostbite. I. Modeling aspects.

Tyler Fara and Malgorzata Peszynska*

Department of Mathematics, Oregon State University, 2000 S.W. Campus Way, Corvallis, OR 97331, USA

* **Correspondence:** Email: mpesz@oregonstate.edu; Tel: 541-737-9847.

Abstract: We propose a new bioheat model for thermoregulation in the human body in response to cold environments, with emphasis on hypothermia and frostbite in exposed extremities. The model couples the bioheat transfer equation in the extremity with a differential equation that describes the core temperature. We used simulations to illustrate the connection between microscale vascular exchange and the effective perfusion term in the bioheat transfer equation. The nonlinear coupling proposed here incorporates physiologically motivated feedback laws for local and reflex vasoconstriction, as well as heat exchange with the environment. We illustrated the model numerically with realistic scenarios of thermoregulation regarding the thermal response of the body, which involves preservation of core temperature despite an increased frostbite risk. The model provides a robust framework for predictive studies of cold-induced injuries.

Keywords: Thermoregulation; frostbite; hypothermia; coupled system; nonlinear boundary conditions; finite elements; multiscale modeling

1. Introduction

Modeling heat transfer within biological tissues poses substantial mathematical and computational challenges due to the complex, interconnected, and multiscale nature of human physiology.

Accurate modeling of body thermoregulation in response to cold and, in particular, of hypothermia and cold-related frostbite injuries to the extremities requires capturing the dynamics of heat exchange between the body's core and peripheral regions such as the hands or feet. These thermoregulatory processes involve intricate interactions between metabolic heat production, vascular heat convection, and environmental heat losses through conduction, convection, radiation, and evaporation. In fact, the body faces two threats: hypothermia affecting the body's core, and frostbite affecting the extremities. Interestingly, the extent of the latter can be partially attributed to the body's strategy to prevent the

former. This paper is devoted to the modeling of both threats.

Early bioheat transfer models, notably the Pennes model from [1], represent heat convection through the vascular system with an averaged perfusion rate in the heat exchange term $A_b(\theta - \theta_b)$, where θ and θ_b are the tissue and blood temperature, respectively, and $A_b = \rho_b c_b \omega_b$ is the product of blood density, specific heat, and volumetric flow rate coefficients, respectively. Other early models, such as [2, 3], attempted to explicitly account for bulk convective effects. In particular, in [3], the term $\rho_b c_b \omega_b(\theta - \theta_b)$ was replaced by $\rho_b c_b U_h \cdot \nabla\theta$, where U_h is a certain weighted average of microscopic blood flow velocities. Later, the authors of [4] were among the first to attempt to incorporate the effects of microvascular physics of perfusion; their formulation of the bioheat transfer equation includes both a perfusion term akin to that in [1] and a convection term as in [3].

That work was followed by [5, 6], which sought a rigorous explanation of the term $A_b(\theta - \theta_b)$ by developing its connection to the microscale structure of vasculature within tissues using two-scale asymptotic homogenization. In particular, in [5], it was proved under the assumption of a periodically distributed vascular network that the homogenized limit closely resembles the Pennes bioheat equation, including the term $A_b(\theta - \theta_b)$. However, the factor A_b is related to the geometry of the microvasculature rather than the material properties and flow rate of blood. Notably, the homogenized model in [5] is stationary. Some work has been done to extend the result of [5] to the parabolic setting, for example, [6]. In Section 2 of this paper, we postulate another such parabolic extension and illustrate this extension and the connection between the microstructure and $A_b(\theta - \theta_b)$ using numerical examples.

In turn, another family of models in the work of Quarteroni et. al. [7] describe fluid flow through vascularized tissue by treating vasculature as a coupled continuum–discrete network. Vascularized tissue is represented as a series of 1D "cracks", which represent the large blood vessels distributed throughout a 3D porous continuum, with the pore-space representing microvasculature and the solid matrix representing the solid tissue. In [8], a mixed finite element discretization of such systems was described, while [9] provided a finite difference discretization. A method for overcoming the computational challenges involved in using 1D sources was presented in [10]. These models inform our general understanding of tissue and vascular networks.

We also note that in porous media literature, terms similar to $A_b(\theta - \theta_b)$ are used to model overlapping continua, where θ_b solves a separate PDE, which captures the different dynamics of θ and θ_b; see the well-known Barenblatt model [11]. More recently, [12] described a multiscale model for heat transport in a doubly porous composite medium made of two interwoven high-conductivity flow paths separated by a thin exchange layer, representing the kind of highly heterogeneous microgeometry found, for example, in vascularized media. By applying two-scale homogenization, the authors rigorously derived a distributed microstructure model that collapses, in the quasi-static limit, to an anisotropic double-diffusion system with an explicit inter-continuum transfer coefficient, thereby furnishing a first-principles justification of the classical Rubinstein–Barenblatt equations for coupled continua. See also [13], in which a two-grid finite element discretization of the double-diffusion system was formulated and a numerical comparison between the micro and macro model was performed. The analogy between the double-diffusion system and the bioheat model was explored in [14].

Exposure to extreme cold or heat can significantly change the physical properties of tissue, either by freezing (as in frostbite) or melting (as in, e.g., tumor ablation). Models that incorporate such changes can be found in, e.g., [15] for freezing or [16] for melting/ablation. We do not address this here.

In this paper, we focus on the dynamic coupling between peripheral and core body temperatures.

The models mentioned above only describe the temperature at every point x. In turn, the dynamic coupling between body compartments was discussed in the pioneering work of Stolwijk and Hardy [17, 18]. This model is called the 25-node model since it divides the body into 25 lumped-parameter compartments, including a centralized blood compartment that facilitates energy exchange between the other 24 compartments. Many thermoregulation models have followed, most of which are either lumped-parameter models or use idealized shapes (cylinders, spheres, circular cones, etc.) to represent the different body parts; see [19] for a review. More recently, whole-body finite element thermoregulation models based on meshes reconstructed from high-resolution MRI data have been developed; see, e.g., [20]. Such a model, however, is extremely complex computationally (see the information provided in [20]).

In this paper, we propose a new coupled PDE-ODE system specifically designed to model the onset of hypothermia and frostbite during extreme cold exposure. We note that our model was developed independently of that in [20]. To focus on the dynamics of energy exchange between the core and extremities during extreme cold exposure, we consider a two-compartment model with an ODE representing the temperature in a well-insulated body core and a bioheat transfer PDE representing the temperature in an extremity, which allows for the spatial resolution necessary to track frostbite during cold exposure.

Specifically, let $\Omega \subset \mathbb{R}^d$ with $d \in \{2, 3\}$ represent an exposed extremity (e.g., a hand) and let the rest of the body be represented by a zero-dimensional compartment. On time interval $J = (0, T]$, we seek $u : \Omega \times J \to \mathbb{R}$ in the hand and $v : J \to \mathbb{R}$ in the core, such that

$$\begin{aligned} c(x)\,\partial_t u - \nabla \cdot (k(x)\nabla u) + r(x,t,u,v) &= f, \quad \text{in } \Omega \times J, && \text{(1.1a)} \\ k(x)\frac{\partial u}{\partial n} &= \alpha(x,t,u,v), \quad \text{on } \partial\Omega \times J, && \text{(1.1b)} \\ u(x,0) &= u_{\text{init}}, \quad x \in \Omega. && \text{(1.1c)} \end{aligned}$$

In turn, we postulate that the function $v = v(t)$ satisfies

$$\begin{aligned} \kappa\frac{dv}{dt} + s(t, v, \langle u\rangle_\Omega) &= g, \quad 0 < t \le T, && \text{(1.2a)} \\ v(0) &= v_{\text{init}}, && \text{(1.2b)} \end{aligned}$$

where $\langle u\rangle_\Omega$ is the average of u over Ω; the other coefficients and data for this model will be described in Section 4. Through the (potentially) nonlinear coupling coefficients $r(\cdot)$ and $s(\cdot)$, this system explicitly incorporates physiological feedback mechanisms, such as local and reflex vasoconstriction responses, as functions of tissue and core temperatures. In Section 4, we will describe several choices for $r(\cdot)$, $s(\cdot)$, and $\alpha(\cdot)$, including a variant based on the model from [17, 18, 20]. In Section 5, we will demonstrate the model and these choices numerically, and compare some of these choices to experimentally obtained physiological data.

Our model also has a robust mathematical and computational foundation. In a forthcoming paper [21], we prove its stability and we propose its numerical discretization with first-order Galerkin finite elements and backward Euler time stepping and prove *a priori* error estimates for the system, given mild assumptions on $r(\cdot)$, $s(\cdot)$, and $\alpha(\cdot)$. Of note, all the choices of $r(\cdot)$, $s(\cdot)$, and $\alpha(\cdot)$ illustrated in this present paper fit these assumptions.

The main result of the present paper is that our proposed model is capable of replicating physiologically realistic scenarios under various thermal exposures, which we demonstrate through a series of

simulations. These results not only validate the theoretical constructs of the model but also highlight its potential applicability in medical predictions and interventions related to cold-induced injuries.

1.1. Outline

The paper is organized as follows: Section 2 introduces the bioheat models and provides illustrations of the term $A_b(\theta - \theta_b)$ using microscale and macroscale simulations. Section 3 provides essential physiological information on a body's thermoregulation and hypothermia. Section 4 then explains the coupled PDE-ODE model in detail. In Section 5, we illustrate our model through numerical simulations under various physiologically relevant scenarios and compare simulations of our model with experimentally obtained data. Section 6 explores the sensitivity of the model to various data.

1.2. Mathematical notation

Let $\Omega \subset \mathbb{R}^d$, $d \in \{2, 3\}$, be an open bounded Lipschitz domain with boundary $\partial\Omega$, with $x = (x_1, \ldots, x_d) \in \Omega$. Let also $t \in J = (0, T]$ be the time variable. Let $\partial_i\varphi, \partial_t\varphi$ denote the partial derivative of φ with respect to x_i and time t, and let $\nabla\phi = (\partial_1\phi, \ldots \partial_d\phi)$. All derivatives are in the sense of distributions.

We will follow the usual notation of Lebesgue spaces L^p and Sobolev spaces H^k and H^1_0 from [22]. In particular, let $L^2(\Omega), L^2(\partial\Omega)$ be associated with the inner product and the norms

$$(\varphi, \psi) = \int_\Omega \varphi\psi \, dx, \qquad (\varphi, \psi)_{\partial\Omega} = \int_{\partial\Omega} \varphi\psi \, ds, \qquad \|\psi\|^2 = (\psi, \psi), \qquad \|\psi\|^2_{\partial\Omega} = (\psi, \psi)_{\partial\Omega}.$$

We denote by $|\Omega|$ the Lebesgue measure of Ω and denote by $|\partial\Omega|$ the $(d\text{-}1)$-dimensional surface measure of $\partial\Omega$. For $u \in L^1(\Omega)$, we denote its average as

$$\langle u \rangle_\Omega := \frac{1}{|\Omega|} \int_\Omega u(x) \, dx.$$

2. Illustration of homogenized energy exchange

In this section, we briefly review the bioheat models derived by Pennes in [1] and by a homogenization-based approach for an elliptic PDE model in [5]. We postulate a transient extension to the latter model that makes the PDE parabolic, and we illustrate the heat exchange term in this equation, as well as the relationship between the micro- and macroscale models.

In this section, we work in a domain Ω_{body} representing the tissue in the human body.

2.1. The bioheat transfer equation

The heat equation is a well-known PDE derived from energy conservation coupled with Fourier's law of heat conduction, and solved for the temperature variable. In any material, the heat (thermal energy) can also be convected by fluids and can be produced, consumed, or lost due to, e.g., radiation.

The heat in Ω_{body} is produced by the metabolism and is transferred by conduction and convection through the vasculature, i.e., the network of blood vessels that has a complex, interconnected, and multiscale nature. In particular, large blood vessels bifurcate into a complicated web of arterioles,

Table 1. Parameters in Pennes equation (2.1). The unit of ω_b should be interpreted as liter of blood flow per liter of tissue per second.

symbol	meaning	units	approx. value	source
c_{tissue}	tissue specific heat	J kg^{-1} °C^{-1}	2274 to 3617	[24]
ρ_{tissue}	tissue density	kg m^{-3}	911 to 1079	[24]
$c = c_{\text{tissue}}\,\rho_{\text{tissue}}$	tissue volumetric heat capacity	J °C^{-1} m^{-3}		
k	tissue thermal conductivity	W m^{-1} °C^{-1}	0.21 to 0.57	[24]
f	tissue heat sources (e.g., metabolism)	W m^{-3}	0 to 1,200	[25]
c_b	blood specific heat	J kg^{-1} °C^{-1}	3617	[24]
ρ_b	blood density	kg m^{-3}	1050	[24]
ω_b	blood specific flow rate	s^{-1}	0 to 5.0×10^{-3}	[23]
$A_b = c_b\,\rho_b\,\omega_b$	heat transfer coefficient	W m^{-3} °C^{-1}		
θ_b	blood temperature	°C		

capillaries, and venules, together called the *microvasculature*. In principle, one can attempt to approximate the convective effect of blood flow on tissue temperature, but the complexity of accounting for the numerous small blood vessels across all scales is too large to be practical.

We recall two models that have tackled this exchange.

2.1.1. The Pennes bioheat model

The bioheat transfer equation describing the tissue temperature $\theta(x, t)$ depending on the temperature of the circulating blood θ_b proposed in [1] is as follows:

$$c\frac{\partial\theta}{\partial t} - \nabla\cdot(k\nabla\theta) + A_b(\theta - \theta_b) = f, \qquad x \in \Omega_{\text{body}}, \qquad t > 0. \tag{2.1}$$

This linear parabolic equation includes physical parameters $c = c(x), k = k(x)$, whose values depend on the type of tissue at x (e.g., bone, skin, or internal organs) and are given in Table 1. Of particular interest is the coefficient $A_b = c_b\rho_b\omega_b$, in the term $A_b(\theta - \theta_b)$ which is postulated to approximate the effect of blood convection through the vasculature on the tissue temperature through the rate of energy transfer between blood and tissue in a specific volume of tissue. The factor ω_b represents the volumetric blood perfusion rate and varies greatly with tissue type, thermal state, and activity rate, with greater ω_b directly proportional to greater approximate convective energy transfer. For example, in the hand tissue, values of $\omega_b \in [3.3 \times 10^{-5}, 5.0 \times 10^{-3}]$ were given in [23]. We note that this data range spans two orders of magnitude; this wide range of values motivates some of our modeling postulates to be developed.

For well posedness, the model (2.1) must be supplemented with some boundary and initial data.

2.2. Explanation of the heat exchange term through homogenization

In [1], the term $A_b(\theta - \theta_b)$ and the value of A_b are postulated heuristically. However, its role can be explained through homogenization theory, as shown in [5].

Homogenization theory is a powerful mathematical tool that helps to connect the scales present in PDE models. In one of the first monographs devoted to homogenization [26], one learns how to derive

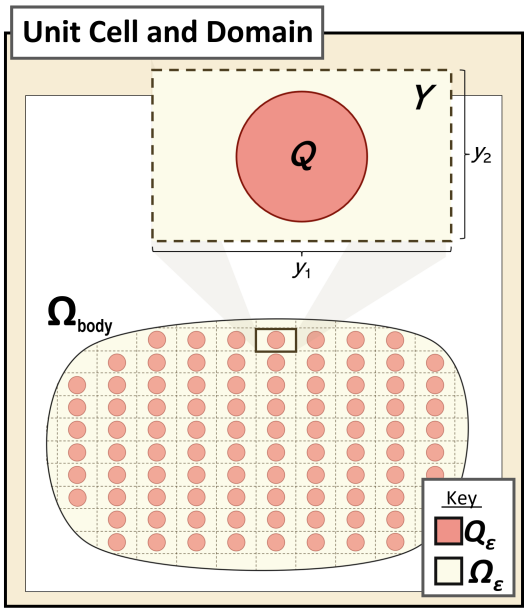

Figure 1. Domain $\Omega_{\text{body}} = \Omega_\varepsilon \cup Q_\varepsilon$ for the microscale model in [5], which is a union of scaled copies of the unit cell Y, which features an inclusion Q representing the pores (small blood vessels) in Q_ε, with solid tissue in $Y \setminus Q$ and Ω_ε.

an effective PDE model posed at a macroscale, e.g., on a scale of order of meters, from a microscale problem defined at, say, a scale of millimeters. A classical and well-explored example is that of an elliptic (stationary) PDE for heat conduction in a composite material with periodically varying coefficients at a microscale. After averaging, one obtains a macroscale PDE with effective coefficients, which are calculated from those at the microscale coefficients through an auxiliary problem. Another example is that of a PDE defined on a domain with perforations, such as the case in [5]. The mathematical techniques to derive the effective model and its coefficients include asymptotic expansions as well as the theory of weak and two-scale convergence.

For parabolic problems, especially those with coefficients of largely disparate values, for a good agreement between macroscale solutions and the averages of microscale solutions, one may incorporate additional terms in the homogenized PDE, or maintain the two-scales as proved in [12] and illustrated in [13].

Below, we focus on the specific application of homogenization theory to the blood perfusion. In [5], the following stationary microscale problem is considered

$$\begin{aligned} -\Delta\theta_\varepsilon &= f_\varepsilon, \quad \text{in } \Omega_\varepsilon, \\ \theta_\varepsilon &= 0, \quad \text{on } \partial\Omega, \\ -\frac{\partial\theta_\varepsilon}{\partial n} &= \varepsilon a(\theta_\varepsilon - \theta_b^\varepsilon), \quad \text{on } \partial Q_\varepsilon, \end{aligned}$$

where $\Omega_\varepsilon = \Omega_{\text{body}} \setminus Q_\varepsilon$ represents tissue perforated by small blood vessels represented by Q_ε and arranged periodically. The domain $Q \subset Y$ is the inclusion from which Q_ε is defined, and Y is the periodic unit cell, with $Y^* = Y \setminus Q$; see Figure 1. The heat conductivity is $k = 1$ or is absorbed in f_ε.

The outward normal vector n is involved with the Robin exchange term between the perforations in the microvasculature and the tissue on ∂Q_ε, with the coefficient εa representing the scaled rate of

energy transfer across the vessel walls ∂Q_ε per degree difference between tissue temperature θ_ε and blood temperature θ_b^ε.

The results of [5] show that the projections of θ_ε to $H_0^1(\Omega)$ converge weakly in $H_0^1(\Omega)$ to the solution θ to the macroscale problem

$$-\nabla\cdot(\mathcal{K}\nabla\theta) + a\frac{|\partial Q|}{|Y|}(\theta-\theta_b) = \frac{|Y^*|}{|Y|}f, \quad \text{in } \Omega, \tag{2.3a}$$

$$\theta = 0, \quad \text{on } \partial\Omega. \tag{2.3b}$$

Here, θ_b is the weak limit in $H_0^1(\Omega)$ of θ_b^ε, f is the limit in $L^2(\Omega)$ of f_ε, and $\mathcal{K} = (k_{ij})_{ij}$ is the standard homogenized (upscaled) conductivity, a positive definite matrix calculated by homogenization using an auxiliary PDE; details are given in Section 2.3.

We see that (2.3) is a stationary version of (2.1). The Helmholtz exchange term $a\frac{|\partial Q|}{|Y|}(\theta-\theta_b)$, derived from homogenization, involves the product of a and the specific surface area factor $|\partial Q|/|Y|$ of the microvessel Q. Its role is similar to $A_b = c_b\rho_b\omega_b$ in (2.1); both represent the volumetric rate at which heat is exchanged between blood and tissue. Because perfusion is governed chiefly by vasoconstriction or dilation of precapillary arterioles [25, 27], widening these vessels can be viewed either as increasing the perfusion rate ω_b in (2.1) or as enlarging the interfacial-area ratio $|\partial Q|/|Y|$ in (2.3), with both interpretations leading to a larger energy-exchange term.

We now explain the connection between the microstructure and macroscale parameters. Assume that $\Omega \subset \mathbb{R}^2$ is circular with radius R. We can calculate $R = |\partial Q|/2\pi$, and the radius of each perforation in Q_ε is εR. This microstructure radius εR links the scale parameter ε and the ratio $|\partial Q|/|Y|$. When $\varepsilon \to 0$, we have more, smaller vessels perfusing the tissue, while $|\partial Q|/|Y|$ represents the vessels' relative dilation or constriction within the tissue. The effect of changing either ε or $|\partial Q|/|Y|$ is illustrated in Section 2.3.1.

We note that homogenization theory does not require that Q be circular. It is, however, convenient to assume so in the numerical illustrations below.

2.3. Micro- to macroscale simulations inspired by [5]

We illustrate now the effect of the exchange term $A_b(\theta-\theta_b)$, where $A_b = a\frac{|\partial Q|}{|Y|}$ is derived by homogenization.

Our illustrations extend the theoretical results of [5] in several ways. We treat the transient version of the problem. We also partition $\partial\Omega_{\text{body}}$ into $\partial\Omega_D$, where we impose a Dirichlet condition θ_D, and $\partial\Omega_N$, where we impose a homogeneous Neumann condition. Our model uses the physical parameter k, which was set to unity in [5], as well as the parameter c in a term absent in [5]

Let $\Omega_{\text{body}} = (0, x_1') \times (0, x_2')$, let $Y = (0,1)^2$, and let Q be a disk centered in Y representing a perforation. For $\varepsilon > 0$, define $\tau(\varepsilon Q) := \bigcup_{\ell\in\mathbb{Z}^2} \varepsilon(\ell + Q)$, $Q_\varepsilon := \Omega_{\text{body}} \setminus \tau(\varepsilon Q)$, and $\Omega_\varepsilon := \Omega_{\text{body}} \setminus \overline{Q_\varepsilon}$. Let ε be chosen so that $\overline{\tau(\varepsilon Q)} \cap \partial\Omega_{\text{body}} = \varnothing$. See Figure 1 for an illustration of Y, Q, Q_ε, and Ω_ε in a generic domain. Let $\partial\Omega_{\text{body}} = \overline{\partial\Omega_D} \cup \overline{\partial\Omega_N}$ where $\partial\Omega_D \cap \partial\Omega_N = \varnothing$.

We consider the microscale problem on a domain with perforations Q_ε:

$$c\frac{\partial\theta_\varepsilon}{\partial t} - \nabla\cdot(k\,\nabla\theta_\varepsilon) = f_\varepsilon, \quad \text{in } \Omega_\varepsilon \times (0,T], \tag{2.4a}$$

$$\theta_\varepsilon = \theta_D, \quad \text{on } \partial\Omega_D \times (0,T], \tag{2.4b}$$

$$\frac{\partial \theta_\varepsilon}{\partial n} = 0, \quad \text{on } \partial\Omega_N \times (0,T], \tag{2.4c}$$

$$-k\frac{\partial \theta_\varepsilon}{\partial n} = \varepsilon a_b(\theta_\varepsilon - \theta_b^\varepsilon) \quad \text{on } \partial Q_\varepsilon \times (0,T], \tag{2.4d}$$

$$\theta_\varepsilon(x,0) = \theta_{\text{init}}^\varepsilon(x), \quad \text{in } \Omega_\varepsilon. \tag{2.4e}$$

We postulate that the solutions θ_ε are well approximated by the solution θ to the macroscale problem:

$$c\frac{|Y^*|}{|Y|}\frac{\partial \theta}{\partial t} - \nabla\cdot(\mathcal{K}\nabla\theta) + a_b\frac{|\partial Q|}{|Y|}(\theta - \theta_b) = \frac{|Y^*|}{|Y|}f, \quad \text{in } \Omega\times(0,T], \tag{2.5a}$$

$$\theta = \theta_D, \quad \text{on } \partial\Omega_D \times (0,T], \tag{2.5b}$$

$$\frac{\partial \theta}{\partial n} = 0, \quad \text{on } \partial\Omega_N \times (0,T], \tag{2.5c}$$

$$\theta(x,0) = \theta_{\text{init}}(x), \quad \text{in } \Omega, \tag{2.5d}$$

where, for simplicity, we assume that $c, k, a_b, \theta_b^\varepsilon$, and θ_b are positive constants, and $\theta_b^\varepsilon = \theta_b$ for all choices of ε. The tensor $\mathcal{K} = (k_{ij})_{ij}$ is given by

$$k_{ij} = k\left(\frac{|Y^*|}{|Y|}\delta_{ij} - \frac{1}{|Y|}\int_{Y^*}\frac{\partial \chi^j}{\partial y_i}\,dy\right), \tag{2.6}$$

where δ_{ij} is the Dirac delta, and functions χ^j are the solutions to an auxiliary PDE

$$-\Delta_y \chi^j = 0, \quad \text{in } Y^*, \tag{2.7a}$$

$$\frac{\partial(\chi^j - y_j)}{\partial n} = 0, \quad \text{on } \partial Q, \tag{2.7b}$$

$$\chi^j \quad Y\text{-periodic}, \tag{2.7c}$$

where $y = (y_1, y_2) = x/\varepsilon$, and y_j denotes the j-th coordinate function. We refer to [13, 26, 28] for the theoretical derivations of the formulas (2.6) and (2.7) for these homogenized coefficients.

We illustrate the microscale and macroscale solutions numerically. For numerical illustrations, we discretize (2.4), (2.5), and (2.7) using P1 Lagrange finite elements (mesh size $h = x_1' \times 10^{-6}$) with backward Euler time stepping.

We set up two scenarios: in Section 2.3.1, we consider the problem with a constant θ_b and physiologically relevant coefficients. In Section 2.3.2, we consider a problem with strongly varying (oscillating) θ_b and with unit coefficients.

2.3.1. Scenario with physiologically meaningful data

Let $x_1' = 0.03$, $x_2' = 0.01$ so that Ω_{body} represents a rectangular 1 cm × 3 cm patch of tissue. Let

$$\partial\Omega_D = \{x \in \partial\Omega_{\text{body}} : x_1 = 0 \text{ or } x_1 = x_1'\},$$
$$\partial\Omega_N = \partial\Omega_{\text{body}} \setminus \partial\Omega_D,$$

and $T = 1000$ s with timestep $\tau = 1$ s. We use physiologically relevant data, i.e., $c = 3.5\times10^3$ J kg^{-1} °C^{-1}, $k = 0.42$ W m^{-1} °C^{-1}, $a_b = 4.2\times10^3$ W m^{-3} °C^{-1}, $\theta_b = 37$ °C. These data are similar to those used in other examples in this paper; see Table 7.

Table 2. Convergence rates for experiments in Section 2.3.1.

$\lvert\partial Q\rvert / \lvert Y\rvert = 0.5$				$\lvert\partial Q\rvert / \lvert Y\rvert = 1.0$				$\lvert\partial Q\rvert / \lvert Y\rvert = 1.5$			
ε	$\mathrm{err}_{\mathrm{abs}}$	$\mathrm{err}_{\mathrm{rel}} \times 10^{-2}$	rate	ε	$\mathrm{err}_{\mathrm{abs}}$	$\mathrm{err}_{\mathrm{rel}} \times 10^{-2}$	rate	ε	$\mathrm{err}_{\mathrm{abs}}$	$\mathrm{err}_{\mathrm{rel}} \times 10^{-2}$	rate
1	1.07	1.67	–	1	2.92	4.75	–	1	4.84	8.33	–
1/3	0.562	8.85	0.587	1/3	1.74	2.83	0.470	1/3	2.96	5.09	0.448
1/6	0.359	5.66	0.646	1/6	1.10	1.79	0.659	1/6	1.91	3.28	0.637
1/9	0.250	3.94	0.893	1/9	0.811	1.32	0.759	1/9	1.37	2.36	0.813

This scenario simulates the tissue Ω_{body} touching a cold object on its east edge and connected to the body core on its west edge. Specifically, we let $\theta_{\mathrm{cold}} = -40\ ^\circ\mathrm{C}$, $\theta_{\mathrm{init}} = \theta_b$, and we choose

$$\theta_D = \begin{cases} \theta_b, & x_1 = 0, \\ \theta_{\mathrm{cold}}, & x_1 = x_1'. \end{cases}$$

We simulate solutions to both the microscale and macroscale (homogenized) models. In the microscale problem, the tissue is warmed by perfusing blood through the Robin condition (2.4d). In the macroscale problem, the tissue temperature responds to θ_b through the homogenized bulk energy exchange term $a\frac{|\partial Q|}{|Y|}(\theta - \theta_b)$ given in (2.5a).

The illustration in Figure 2 shows both the effect of changing ε and changing $|\partial Q|/|Y|$. Comparing the left and middle panels, ε is reduced from $\varepsilon = 1$ to $\varepsilon = 1/5$, while $|\partial Q|/|Y| = 1.5$ in both. In both panels, the overall trend of θ and θ_ε is similar. However, with larger $\varepsilon = 1$, θ_ε exhibits noticeable local distortion near the inclusions. With smaller $\varepsilon = 1/5$, these local gradients are reduced, along with the maximum deviation between θ and θ_ε.

Convergence data, presented in Table 2, support this observation. For each choice of $|\partial Q|/|Y| \in \{0.5, 1.0, 1.5\}$ and $\varepsilon \in \{1, \frac{1}{3}, \frac{1}{6}, \frac{1}{9}\}$, we calculate

$$\mathrm{err}_{\mathrm{abs}} = \max_{1\le n\le 1000} \|\theta^n - \theta_\varepsilon^n\|_{L^2(\Omega_\varepsilon)}, \qquad \mathrm{err}_{\mathrm{rel}} = \max_{1\le n\le 1000} \|\theta^n - \theta_\varepsilon^n\|_{L^2(\Omega_\varepsilon)} / \|\theta^n\|_{L^2(\Omega_\varepsilon)}.$$

As expected, these errors decrease as ε decreases, suggesting that the microscale and homogenized temperature fields become increasingly indistinguishable at all measured time points as the characteristic vessel scale ε decreases. Also, the homogenized model accurately represents the effective heat transfer in densely perfused tissue. Moreover, the observed decay of the error as $\varepsilon \to 0$ supports the conjecture that the convergence results proven in [5] for the elliptic formulation may extend to the time-dependent parabolic problem.

Figure 2 also illustrates the effect of $|\partial Q|/|Y|$. The middle panel shows $|\partial Q|/|Y| = 1.5$, and the right panel $|\partial Q|/|Y| = 0.5$, with $\varepsilon = 1/5$ in each. For the choice $|\partial Q|/|Y| = 0.5$, Table 2 again demonstrates good agreement through time between the micro- and macroscale solutions. Reducing $|\partial Q|/|Y|$ to $|\partial Q|/|Y| = 0.5$ causes a reduction in temperature at each comparable point of the domain, compared to $|\partial Q|/|Y| = 1.5$. Physically, this could be interpreted as vasoconstriction resulting in less blood-tissue energy exchange and leading to a reduced tissue temperature.

2.3.2. Scenario driven by an oscillating θ_b, with simplified material constants

We now present a scenario where the microscale solution θ_ε has a local behavior with strong variability but its average is similar to θ. In this scenario, a "pulse" of heat energy imposed by θ_b has a rate

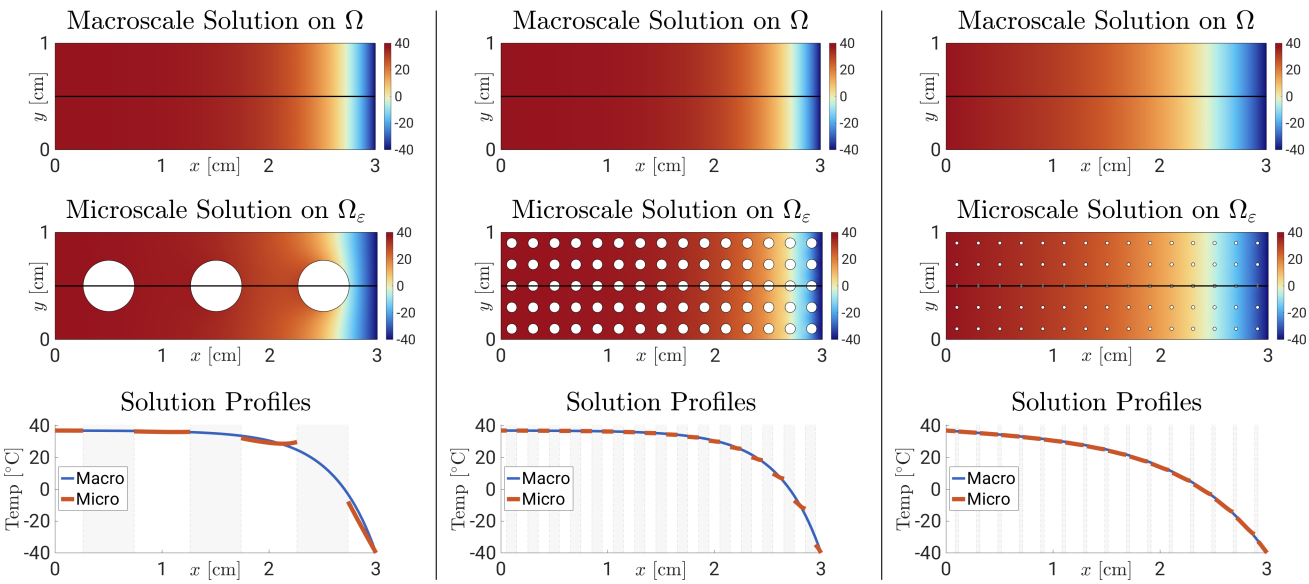

Figure 2. Numerical solutions for Section 2.3.1. Plots of solutions at $t = T$ to macroscale problems (2.5) on Ω (top) and to the corresponding microscale problems (2.4) on Ω_ε (middle) with micro- and macroscale solution profiles (bottom), which represent the solution along the horizontal black line $x_2 = 0.5$. Pictured are the solutions when $\varepsilon = 1$ and $|\partial Q|/|Y| = 1.5$ (left), $\varepsilon = 1/5$ and $|\partial Q|/|Y| = 1.5$ (center), and $\varepsilon = 1/5$ and $|\partial Q|/|Y| = 0.5$ (right). The vertical grey bars in the bottom row correspond to the inclusions, i.e., the regions where the microscale solution is undefined.

that is fast compared to the speed at which heat disperses through Ω_{body}. As a result, the microscale and macroscale solutions are not immediately close. The oscillatory forcing from θ_b in this illustration is not intended to represent a physiological pulse, i.e., a heartbeat, but rather to test the proposed extension (2.5) under strong, rapid transients beyond the scope of the elliptic homogenization theory of [5]. We note, however, that some studies do treat θ_b as a prescribed forcing function, for instance, during therapeutic blood cooling as in [29].

Let $x_1' = 0.01$, $x_2' = 0.01$. Let $\partial\Omega_D = \partial\Omega_{\text{body}}$ so that $\partial\Omega_N = \varnothing$ and use $\theta_D = 0$. Let $T = 1$ with $\tau = 0.01$. We set $c = 10^2$, $k = 0.1$, $a_b = 1$, $f = 0$, $\theta(\cdot, 0) = 0$, $\theta_\varepsilon(\cdot, 0) = 0$. These coefficients are chosen to emphasize the differences between the microscale and homogenized models, rather than for physiological realism.

The focus of this example is on θ_b, which varies significantly with amplitude $A = 50$ and period $P = 1$ according to

$$\theta_b(x, y, t) = A\,\theta_{\text{space}}(x, y)\,\theta_{\text{time}}(t),$$

$$\theta_{\text{space}}(x, y) = \max\left\{0, 1 - \left[(x - x_c)^2 + (y - y_c)^2\right]^{1/2}/R\right\}, \quad \theta_{\text{time}}(t) = \max\{0, \sin(2\pi t/P)\},$$

where $(x_c, y_c) = (0.5, 0.5)$ and $R = 0.4$. We also let θ_b^ε be the trace of this function on ∂Q_ε.

We fix $|\partial Q|/|Y| = 1$, and vary $\varepsilon \in \left\{1, \frac{1}{7}, \frac{1}{11}, \frac{1}{15}\right\}$. Figure 3 shows results at $t = 0.4$, just after the pulse peak and before the delivered heat had sufficient time to diffuse through the microscale domain, thereby highlighting the transient boundary-layer effects present in the microscale model. For all ε, the profile of $\theta(\cdot, t)$ is similar to the profile of θ_b, reflecting that, for the homogenized solution, the

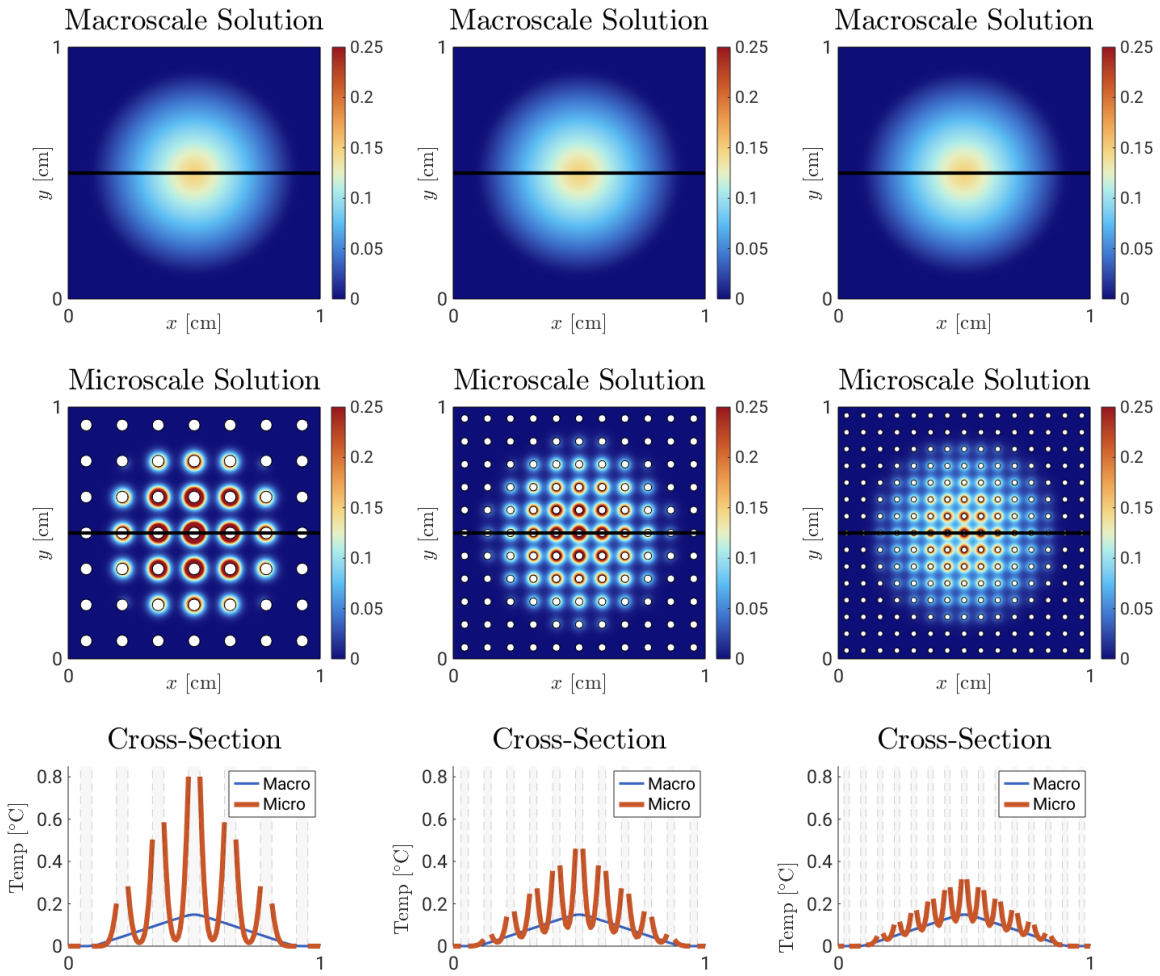

Figure 3. Numerical solutions for experiments in Section 2.3.2 with $\varepsilon = 1/7$ (left), $\varepsilon = 1/11$ (middle), and $\varepsilon = 1/15$ (right). Shown are the macroscale solutions (top row), microscale solutions (middle row), and solution profiles (bottom row), which are taken along the black line depicted in the top and middle rows. In the middle row, we clip the color scale for $\theta_\varepsilon(x)$ at 0.25 to facilitate comparison of the macroscale and microscale plots.

effect of θ_b is distributed evenly within its support in Ω_{body}. However, the microscale solution θ_ε shows large spikes, where ∂Q_ε is within the support of θ_b, which appear because the heat builds up along ∂Q_ε faster than it can dissipate into Ω_ε. As $\varepsilon \to 0$, the overall profile of θ_ε increasingly resembles that of θ, although localized oscillations near the micro-interfaces remain visible.

While the parameters in this example were chosen for illustration rather than realism, time-dependent effects of this kind may naturally arise in physiological settings. This example thus aims to illustrate potential limitations of the postulated time-varying extension given by equations (2.5) when very strong transients are present.

Table 3. Stages and symptoms of hypothermia; adapted from [30].

v °C	stage	symptoms
33 to 35	mild	muscle weakness, disorientation, extreme vasoconstriction, and shivering
32 to 33	moderate	diminished cardiac output, breathing rate, and shivering
30 to 32	severe	loss of consciousness, imperceptible pulse, shivering stops
28 to 29	death	cardiac fibrillation, usually resulting in death

Table 4. Heat production sources as in [25].

source	energy contribution
basal	85 W
shivering	[0, 350] W
physical activity	[0, 1200] W

3. Temperature regulation in the human body

In this section, we summarize physiological mechanisms involved in human thermoregulation and specifically in the body's responses to cold exposure. We also clarify limitations of existing models and motivate the need for our new model to involve the thermal regulation in the body coupled to that in the extremities (hands and feet) when exposed to the cold.

3.1. Realistic thermal conditions for a human body

We first provide some background based on [25, 30]. The average human body temperature $\theta(t)$ is around ≈ 37 °C in its core, a situation known as *normothermia*. The body cannot tolerate large changes away from normothermia.

In particular, the condition of *hyperthermia*, when $\theta \geq 38$ °C [25], may lead to life threatening heat stroke. In turn, if θ drops below 35 °C, the body enters *hypothermia*, which is of particular interest in this paper. In Table 3, we recall physiological details of this condition.

3.2. General mechanisms of thermoregulation

Now, we revisit the terms in (2.1) as they relate to thermoregulation. The human body attempts to regulate its temperature θ by maintaining a stable heat content $S(t) = \int_V c\rho\theta$ in some arbitrary control volume V, where $c = c(x)$ and $\rho = \rho(x)$, when V contains different tissue types. This is done by balancing metabolic heat production M within V, represented in (2.1) by its density f, against the heat transfer due to conductive fluxes $K = -k\nabla\theta$ and convective fluxes $C = q\theta$ across ∂V; those fluxes associated with the perfusion and blood flow are represented in (2.1) through the exchange term $A_b(\theta-\theta_b)$, with $q \approx \omega_b$. When in contact with the environment, there is also radiation R and evaporation E, represented by boundary conditions [25, 30, 31, 32]. In this paper, we are most interested in the connection between different portions of $S(t)$ and its regulation in the body and in the extremities in near hypothermia conditions.

Heat is brought to the skin by conduction and convection via cutaneous blood flow, with flow rates

Table 5. Blood flow rates ω_b in the hand, foot, and skin, compared to total cardiac output, i.e., the total flow rate leaving the heart. Basal rates are for the body at rest during normothermia. Minimal and maximal rates correspond to extreme hypothermia and hyperthermia, respectively. Units are L min^{-1}.

	hand	foot	skin	total cardiac output
basal	0.026	0.024	0.25	5
minimal	0.0015	0.0017	6 to 8	2.5
maximal	0.11	0.15	∼0	13

given in Table 5. In normothermia, the skin dissipates heat at a rate of ∼100 W, roughly matching the *basal* (typical) metabolic rate M [33]. In hyperthermia, the skin blood flow and sweating increase E until the heat generation and dissipation are equal [33]. For example, a sweat rate of 1 L hr^{-1} leads to E at a rate of 675 W [30].

Hypothermia results if $M < E+R+C+K$ for some time; see Table 3. To prevent hypothermia during cold exposure, the body reduces skin blood flow rate in order to limit R and C, which together constitute about 75% of heat loss [33, 27]. The body also initiates shivering and behavioral changes, i.e., increased physical activity [25, 30]; see Table 4. However, the disorientation at even mild hypothermia may lead to a cessation of physical activity, and the loss of consciousness below 32 °C is accompanied by both complete cessation of shivering and physical activity [30], underscoring that survival of an individual exposed to the cold requires maintaining θ in a narrow window.

3.3. Heat regulation in the core and in the extremities (hands and feet)

Now we discuss different portions of Ω_{body}. To regulate the core body temperature in addition to the mechanisms listed in Section 3.2, the body utilizes cutaneous blood flow to facilitate environmental energy exchange prevalent in the extremities. The extremities (hands and feet) substantially facilitate this thermal regulation, especially when the body's core is insulated with protective clothing.

The hands and feet are excellent radiators, evaporators, and insulators, having a significantly larger surface-area-to-mass ratio (980 cm^2 kg^{-1}) compared to that of the body (240 cm^2 kg^{-1}) [23]. Specialized vasculature allows a wide range of volumetric blood flow rates within the hands and feet, which allows a wide range of energy exchange rates with the environment; see Tables 5 and 6.

Therefore, we focus on the core Ω_{core} (trunk, head, and limbs) and the extremities (hands and feet) Ω (note that we use no subscript for simplicity of subsequent notation). We set

$$v(t) \approx \langle \theta(\cdot, t) \rangle_{\Omega_{\text{core}}}, \quad u = \theta|_{\Omega}. \tag{3.1}$$

We provide an illustration in Figure 4.

We are primarily interested in the energy exchange between $v = v(t)$ and $u = u(x,t)$, $x \in \Omega$. In model development, we first argue that the heat transfer within Ω_{core} is fast relative to that in Ω, so that it makes sense to neglect the effects of heat conduction in Ω_{core}. Second, we believe it is important to model temperature in Ω pointwise, since the extremities are particularly susceptible to the cold due to their distance from the body core and the fact that the hands and feet have little ability to generate heat locally [23].

Table 6. Maximal and minimal energy dissipation rates in the hand and foot [23] with units of W. Rates for R and C correspond to a 1 °C difference between tissue and air.

	hand	foot
Maximal R and C	6.0	8.5
Minimal R and C	below 0.1	below 0.1
Maximal E	67	46
Minimal E	below 0.1	below 0

3.4. Reaction of the body to significant cold exposure

During cold exposure, the body aims to protect its core from hypothermia by drastically reducing the blood flow within the extremities. In particular, this process limits the cooling effects of severely cooled blood returning from extremities. However, this strategy creates the risk of a cold-induced injury called *frostbite* caused by tissue freezing [34], which can develop in a matter of minutes or even seconds [30].

The reduction of blood flow follows from *cutaneous vasoconstriction* of two forms:

1. *Reflex vasoconstriction.* Signals from thermoreceptors in the skin, deep body tissue, and brain aggregate in the posterior hypothalamus, triggering whole-body reflex vasoconstriction, resulting in a systemic reduction of blood flow to the skin and extremities [27, 31, 35]. Venous compliance ("stretchiness") allows storage of blood in deep-body veins during reflex vasoconstriction [23].
2. *Local vasoconstriction.* Local cooling causes local vasoconstriction, which is mediated by several pathways, both neuronal and non-neuronal [31, 33, 35]. In particular, local vasoconstriction is mediated in part by *paracrine* ("local, non-neuronal") signaling within the tissue itself, and thus does not necessarily require input from the nervous system [35].

Reflex and local vasoconstriction accelerate the onset of frostbite by depriving skin of its main heat source (i.e., cutaneous blood flow) [34]. In fact, in [23], the authors demonstrate experimentally that reflex (whole-body) vascular control dominates local vascular control; in particular, for $v < 37.0$ °C, the blood flow through the hand is depressed compared to normal, and increases only slightly as hand temperature $\langle u \rangle_\Omega$ is increased from 6.0 to 40.1 °C.

Below we postulate a model of the dynamics between $u(x, t)$ and $v(t)$.

4. Proposed PDE-ODE model for thermoregulation

The bioheat transfer model (2.1) describes the connection between the tissue temperature $\theta(x, t)$ and the convective effects of blood with temperature θ_b flowing through microvasculature embedded in the tissue. In this paper, we extend this model by focusing on the evolution of, and the relationship between, the local tissue temperature in the extremities and the core body temperature, as driven by thermoregulatory responses to extreme cold that substantially alter blood flow patterns. We postulate our model based on the observations from physiological literature recalled in Section 3.

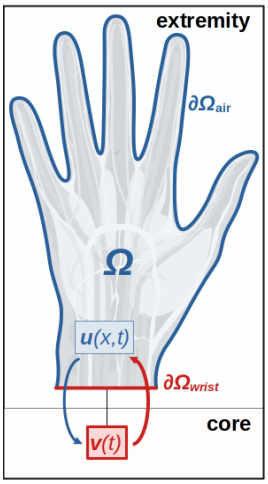

Figure 4. Illustration of blood flow between the body's core and an extremity (hand). $\partial\Omega_{\text{wrist}}$ represents the connection between the hand and the core; $\partial\Omega_{\text{air}}$ represents the portion of the hand exposed to the air. The red arrow shows warm blood flowing to the hand; the blue arrow shows cooled blood returning to the core.

4.1. Two-compartment model

We consider the decomposition of the human body $\overline{\Omega_{\text{body}}} = \overline{\Omega_{\text{core}}} \cup \overline{\Omega}$ into two compartments, where Ω is a set of extremities (hands and feet). For simplicity, we only consider one extremity, the hand Ω. We also treat the core Ω_{core} as a zero-dimensional compartment.

Recalling (3.1), we now postulate the model for the local tissue temperature in the hand $u : \Omega \times J \to \mathbb{R}$ and the core body temperature $v : J \to \mathbb{R}$, which together describe the thermoregulatory response to extreme cold, including the resulting substantial change in blood flow patterns. The model we propose extends (2.1) to a system with nonlinear terms; these extend our previous work [14] on the scalar model.

We consider the following initial boundary value problem for the nonlinear extension of (2.1)

$$\begin{aligned} c(x)\partial_t u - \nabla \cdot (k(x)\nabla u) + r(x,t,u,v) &= f, \quad \text{in } \Omega \times J, && \text{(4.1a)} \\ k(x)\frac{\partial u}{\partial n} &= \alpha(x,t,u,v), \quad \text{on } \partial\Omega \times J, && \text{(4.1b)} \\ u(x,0) &= u_{\text{init}}, \quad x \in \Omega. && \text{(4.1c)} \end{aligned}$$

In turn, we postulate that the function $v = v(t)$ satisfies

$$\begin{aligned} \kappa\frac{dv}{dt} + s(t,v,\langle u\rangle_\Omega) &= g, \quad 0 < t \le T, && \text{(4.2a)} \\ v(0) &= v_{\text{init}}. && \text{(4.2b)} \end{aligned}$$

Based on the discussion in Section 3.3, we disregard conduction in Ω_{core}, assuming it is dominated by the blood flow, and so the average temperature $v(t)$ only responds to the average temperature $\langle u\rangle_\Omega$ in the hand, while it provides the source of blood temperature in the hand. These are modeled by the coupling terms $r(\cdot)$ in (4.1), $s(\cdot)$ in (4.2a), and the boundary term $\alpha(\cdot)$ in (4.1b), which are given below.

The coupling terms $r(\cdot)$, $s(\cdot)$ aim to capture the key features of physiologically realistic energy exchange in the underlying biological system including the vasoconstriction, core-to-extremity heat

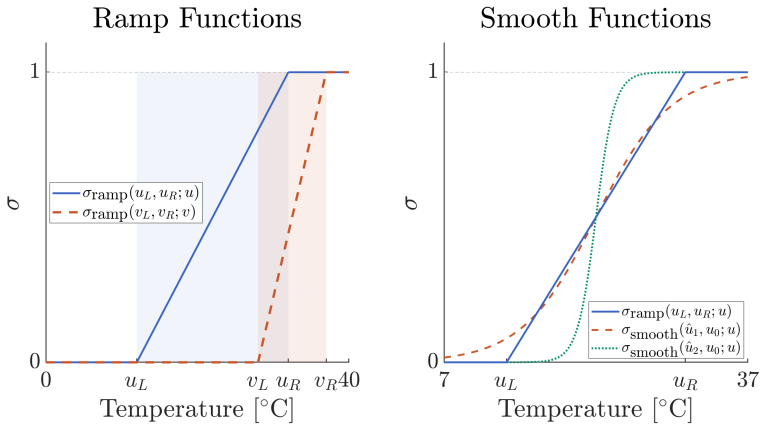

Figure 5. Illustration of activation functions from Section 4.2. Left: plot of $\sigma_{\text{ramp}}(u_L, u_R; u)$, $\sigma_{\text{ramp}}(v_L, v_R; v)$ with u_L, u_R, v_L, v_R as in Table 7. Right: comparison between $\sigma_{\text{smooth}}(\hat{u}_1, u_0; u)$ and $\sigma_{\text{smooth}}(\hat{u}_2, u_0; u)$ against $\sigma_{\text{ramp}}(u_L, u_R; u)$. Here, $u_0 = \frac{1}{2}(u_L + u_R)$ and $\hat{u}_1$ is chosen to minimize the L^2 error between $\sigma_{\text{smooth}}(\hat{u}_1, u_0; u)$ and $\sigma_{\text{ramp}}(u_L, u_R; u)$, and $\hat{u}_2 := 4\,\hat{u}_1$.

exchange, and extremity-to-environment heat exchange discussed in Section 3.3. These can be defined in several ways, and we give some particular choices.

We note that our analysis of this system, which will appear in a future paper [21], allows other choices as long as they satisfy certain smoothness, monotonicity, and bound properties. Our analysis relies only on these mathematical properties rather than on the specific choices made here.

4.2. Auxiliary functions

We begin by defining auxiliary functions σ that satisfy

(P1) $\sigma : \mathbb{R} \to [0, 1]$ is Lipschitz continuous and monotonically non-decreasing on $\mathbb{R}$, and
(P2) $\lim_{x\to+\infty} \sigma(x) = 1$ and $\lim_{x\to-\infty} \sigma(x) = 0$.

Let $a < b, v \in \mathbb{R}$. We define the ramp-like function $\sigma_{\text{ramp}}(a, b; v)$

$$\sigma_{\text{ramp}}(a, b; v) = \frac{v-a}{b-a} H(v-a) - \frac{v-b}{b-a} H(v-b),$$

where H is the Heaviside step function.

Let also $\hat{v} > 0$, $v_0 \in \mathbb{R}$ and define $\sigma_{\text{smooth}}(\hat{v}, v_0; v)$ based on the logistics function

$$\sigma_{\text{smooth}}(\hat{v}, v_0; v) = \frac{1}{1 + e^{-\hat{v}(v-v_0)}},$$

which is a smooth approximation of $\sigma_{\text{ramp}}(a, b; v)$ if $v_0 = \frac{a+b}{2}$.

Clearly, each $\sigma_{\text{ramp}}(a, b; v)$ and $\sigma_{\text{smooth}}(\hat{v}, v_0; v)$ satisfies (P1) and (P2). In addition, $\sigma_{\text{smooth}}(\hat{v}, v_0; v)$ is smooth with the Lipschitz constant dependent on $\hat{v}$. The ramp model reduces to a constant on $(-\infty, a] \cup [b, \infty)$, but the smooth model does not, while it remains bounded. We illustrate these two functions in Figure 5.

4.3. Exchange terms

Now we identify physically motivated choices of $r(\cdot)$, $s(\cdot)$, and $\alpha(\cdot)$. Let $A_b = c_b\rho_b\omega_b$, and let B_b be given, where typically $B_b \ll A_b$ to model the fact that the hand has a much smaller blood volume than the rest of the body [23].

4.3.1. Constant coefficient model

Let

$$r(u, v) = A_b\,(u - v), \quad s(\langle u\rangle_\Omega, v) = B_b\,(v - \langle u\rangle_\Omega). \tag{C}$$

This choice of $r(\cdot)$ is the same as in (2.1), and $s(\cdot)$ represents the linear Fourier condition.

4.3.2. Ramp models

Let $u_L < u_R$ and $v_L < v_R$ be given. We define three variants of $r(\cdot)$ and $s(\cdot)$.

$$\begin{cases} r = A_b\,\sigma_{\text{ramp}}(v_L, v_R; v)\,(u - v), \\ s = B_b\,\sigma_{\text{ramp}}(v_L, v_R; v)\,(v - \langle u\rangle_\Omega), \end{cases} \tag{R1}$$

$$\begin{cases} r = A_b\,\sigma_{\text{ramp}}(u_L, u_R; u)\,(u - v), \\ s = B_b\,\sigma_{\text{ramp}}(u_L, u_R; \langle u\rangle_\Omega)\,(v - \langle u\rangle_\Omega), \end{cases} \tag{R2}$$

$$\begin{cases} r = A_b\,\sigma_{\text{ramp}}(u_L, u_R; u)\,\sigma_{\text{ramp}}(v_L, v_R; v)\,(u - v), \\ s = B_b\,\sigma_{\text{ramp}}(u_L, u_R; \langle u\rangle_\Omega)\,\sigma_{\text{ramp}}(v_L, v_R; v)\,(v - \langle u\rangle_\Omega). \end{cases} \tag{R3}$$

The models (R1), (R2), and (R3) describe the effects of the body's independent systemic and local thermoregulation mechanisms described in Section 3.4.

In particular, the function $r(\cdot)$ in (R3) is the most general: if $u(x, t) < u_R$ at some $x \in \Omega$, the heat exchange between the tissue and blood is suppressed near that point. Similarly, the exchange of heat is suppressed throughout Ω if $v(t) < v_R$. In turn, $s(\cdot)$ in (R3) uses average hand temperature $\langle u\rangle_\Omega$ to approximate the temperature of the blood returning to the body from the hand. With this, we postulate that reduced warm blood flow from the core to the hand corresponds to the reduced cooled return flow. In fact, in experiments, we take $B_b = 0.07A_b$ to account for the fact that the hand contains about 7% of total blood volume [23].

The models (R1) and (R2) are special cases of (R3) when u_R and v_R are chosen significantly below the expected range of u and v, respectively. Their use allows isolating the effects of the systemic or local thermoregulation, respectively.

The models (R1) through (R3) reduce to case (C) when both $u(x, t) > u_R$ and $v(t) > v_R$.

4.3.3. Smooth models

Let $\hat{u}, u_0$ and $\hat{v}, v_0$ be given. We define smooth versions of (R1), (R2), and (R3).

$$\begin{cases} r = A_b\,\sigma_{\text{smooth}}(\hat{v}, v_0; v)\,(u - v), \\ s = B_b\,\sigma_{\text{smooth}}(\hat{v}, v_0; v)\,(v - \langle u\rangle_\Omega), \end{cases} \tag{S1}$$

$$\begin{cases} r = A_b\, \sigma_{\text{smooth}}(\hat{u}, u_0; u)\,(u - v), \\ s = B_b\, \sigma_{\text{smooth}}(\hat{u}, u_0; \langle u \rangle_\Omega)\,(v - \langle u \rangle_\Omega), \end{cases} \tag{S2}$$

$$\begin{cases} r = A_b\, \sigma_{\text{smooth}}(\hat{u}, u_0; u)\, \sigma_{\text{smooth}}(\hat{v}, v_0; v)\,(u - v), \\ s = B_b\, \sigma_{\text{smooth}}(\hat{u}, u_0; \langle u \rangle_\Omega)\, \sigma_{\text{smooth}}(\hat{v}, v_0; v)\,(v - \langle u \rangle_\Omega). \end{cases} \tag{S3}$$

The term $r(\cdot)$ in (S3) behaves similarly to (R3) and models the effects of the exchange of heat between Ω_{body} and Ω, which is significantly suppressed below v_R, u_R. The models (S1) and (S2) play the same role for (R1) and (R2), respectively.

4.3.4. SHC model

Now we consider a heuristic model proposed in [17, 18], which we adopt to define the terms $r(\cdot)$ and $s(\cdot)$; similar as in [20]. We use the acronym SHC to acknowledge the lead authors of these papers. Here, the body attempts to maintain temperatures $u_{\text{set}} = 34\ ^\circ\text{C}$, $v_{\text{set}} = 37\ ^\circ\text{C}$ in Ω, Ω_{core}; this is achieved based on the sensors distributed throughout these compartments. We define

$$\Delta v(t) = v(t) - v_{\text{set}}(t) \quad \text{and} \quad \Delta u(x,t) = u(x,t) - u_{\text{set}}(x,t),$$

and with this

$$\begin{cases} r = \rho_b c_b\, \omega_s(u, v)\,(u - v), \\ s = 0.02 \rho_b c_b\, \omega_s(\langle u \rangle_\Omega, v)\,(v - \langle u \rangle_\Omega), \end{cases} \tag{SHC}$$

where

$$\omega_s(u, v) = \frac{\omega_0 + 0.134\, DI}{1 + CS},$$

where $\omega_0 = 4.39 \times 10^{-4}\ \text{s}^{-1}$ is the normothermic blood flow rate, and the vasodilation term DI and vasoconstriction term CS are given by

$$\begin{aligned} DI &= \max\{0, 28424\, \Delta v + 4870\, \Delta u\}, \\ CS &= \max\{0, -1.1(\Delta v + 3\Delta u)\}. \end{aligned}$$

We note that we copied verbatim the specific coefficient values in the functions DI, CS, and ω_s from [20].

4.4. The model for the boundary conditions on $\partial\Omega$

It remains to define $\alpha(\cdot)$ in (4.1b). We partition $\partial\Omega$ as $\overline{\partial\Omega} = \overline{\partial\Omega_{\text{wrist}}} \cup \overline{\partial\Omega_{\text{air}}}$, where $\partial\Omega_{\text{wrist}}$ and $\partial\Omega_{\text{air}}$ represent the disjoint portions of the boundary of the hand connected to the wrist and exposed to the air, respectively.

In this paper, we consider a linear Robin boundary condition based on Robin conditions

$$\alpha(x, t, u, v) = \begin{cases} a_{\text{wrist}}(u - v), & \text{on } \partial\Omega_{\text{wrist}} \times J, \\ a_{\text{air}}(u - u_{\text{air}}), & \text{on } \partial\Omega_{\text{air}} \times J, \end{cases} \tag{4.3}$$

where $a_{\text{wrist}}, a_{\text{air}} > 0$ and $u_{\text{air}} \in \mathbb{R}$.

4.5. Model summary

The model (4.1)-(4.2) with any of the choices (C) through (S3) complemented by the choice of α in (4.3) is now complete.

5. Numerical results

In this section, we set up and carry out numerical experiments to illustrate the model's dynamic response with physiologically motivated parameters.

5.1. Numerical experiments

Now we conduct simulations designed to illustrate the effects of different choices of energy exchange terms $r(\cdot)$, $s(\cdot)$, $\alpha(\cdot)$.

We consider the following base scenario from a hypothetical real-life situation: A mountaineer in $u_{\text{air}} = -40$ °C attempts self-rescue having lost a glove. We set $u_{\text{init}} = 34$ °C and $v_{\text{init}} = 37$ °C and metabolic rate $g = 700$ W m^{-3}, which is consistent with extensive shivering combined with moderate physical activity [25]. In this scenario, frostbite (i.e., $u < 0$) should begin within minutes [30], but the core body temperature should remain in a survivable range (i.e., $30 < v < 37$) for all $t \in (0, T]$, where $T = 40$ min.

5.1.1. Model data

We let $\Omega \subset \mathbb{R}^2$ be a hand-shaped domain of diameter ≈ 24 cm in height obtained from a photo of one of the authors' hands; see Figure 6. We also have $\partial\Omega = \partial\Omega_{\text{wrist}} \cup \partial\Omega_{\text{air}}$ partitioned as

$$\begin{aligned} \partial\Omega_{\text{wrist}} &= \{(x, y) \in \partial\Omega : y = 0\}, \\ \partial\Omega_{\text{air}} &= \partial\Omega \setminus \partial\Omega_{\text{wrist}}. \end{aligned}$$

We use coefficients from Table 7 and boundary condition (4.3).

5.1.2. Model discretization

In each simulation, we approximate the solution (u, v) to (4.1), (4.2) by (U, V) obtained by discretizing (4.1), (4.2) using P1 Galerkin finite elements and backward Euler timestepping on a triangulation $\mathcal{T}_h$ of Ω created by `Gmsh` with $h \approx 2^{-8}$ (12,081 elements with minimum interior angle of 34°) and $\tau = 1$ s ($N_T = 2400$). The time step is chosen for the reason of accuracy to be studied in [21]. Solutions were generated using `backslashPDE2d`, a MATLAB software package written by the authors.

5.1.3. Solving the nonlinear system

We resolve the nonlinearity in (4.1), (4.2) by Newton's method with iteration lagging. That is, for $(U^{n,k}, V^{n,k})$ representing the k-th iteration of the n-th timestep, we set $(U^{n,0}, V^{n,0}) = (U^{n-1}, V^{n-1})$ where (U^{n-1}, V^{n-1}) represents the resolved solution at the previous timestep. We iterate so that, in the k-th iteration, $V^{n,k-1}$ is used to find $U^{n,k}$, and $U^{n,k}$ is subsequently used to find $V^{n,k}$. We stop the Newton iteration when the absolute error in the L^2 norm is below 10^{-10}.

In practical simulations, we also impose the constraint $v \le v^* := 37$ °C through a constraint operator that is equivalent in implementation to the use of a Lagrange multiplier; see, e.g., [36, 37].

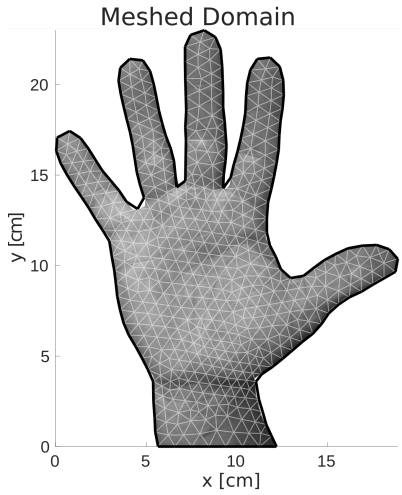

Figure 6. Illustration of Ω with $h = 1$ cm.

5.1.4. Postprocessing the solution

After the simulation is completed, we mark element K as *frostbitten* if $\langle U(t)\rangle_K < 0$ for any $t^n = n\tau \in J$. For each $t^n \in (0, T]$, we define

$$\mathcal{F}(t^n) := \{K \in \mathcal{T}_h : \langle U(t^n)\rangle_K < 0\},$$

and we denote the fraction of cells that are frostbitten at time $t^n \in (0, T]$ by

$$\phi_{\mathrm{FB}}(t^n) := \frac{\sum_{K\in\mathcal{F}(t^n)} |K|}{|\Omega|}. \tag{5.2}$$

5.1.5. Comparison of (C) and (R3)

We first set $r(\cdot)$, $s(\cdot)$ as in case (C) or as in case (R3); see Section 4.2.

In case (C), $v(t)$ traces $\langle u(t)\rangle_\Omega$ closely since there is no regulation of energy exchange between the core and extremity compartments. By contrast, in (R3), an initial drop in $v(t)$ throttles energy exchange, allowing $v(t)$ to recover due to metabolism but causing slightly higher $\phi_{FB}(t)$, cf. (5.2), and lower $\langle u(t)\rangle_\Omega$ at each $t \in (0, T]$. These results are shown in Figure 7.

We comment now on the practical significance of these simulations. While we are not aware of controlled studies of the body's reaction to this scenario, there are case studies from extreme sports accidents wherein an athlete's hand is exposed to extreme cold while the core remains well-insulated, for example [38, 39, 40]. In these works, athletes were accidentally exposed to $u_{\mathrm{cold}} = -3, -25$, or -30 °C for 30 minutes or more. In all cases, the athlete survived the ordeal but sustained moderate to severe frostbite injuries, some requiring amputation. While solutions to models (R3) and (C) both exhibit extensive frostbite, the extreme and rapid drop in $v(t)$ shown in model (C) does not agree with such clinical observations.

5.1.6. Comparison of (R1), (R2), and (R3)

We now compare the different ramp coefficient models by setting $r(\cdot)$, $s(\cdot)$ as in cases (R1), (R2), or (R3).

Table 7. Coefficients for experiments in Section 5 and 6. Empirical parameters are those taken directly from literature. Semi-empirical parameters are those that are chosen from a range of literature values; for example, $g = 700$ W m^{-3} is a heuristic choice, but is chosen from within the range of metabolic heat generation rates reported in [25]. Ad hoc parameters are unique to this model and are therefore not available from literature but rather are chosen by us.

	Coefficient	Value	Units	Motivation
Empirical	c_{tissue}	3.5×10^3	J kg^{-1} °C^{-1}	heat capacity, muscle [24]
	c_b	3617	J kg^{-1} °C^{-1}	heat capacity, blood [24]
	k	0.42	W m^{-1} °C^{-1}	thermal conductivity, muscle [24]
	ρ_b	1050	kg m^{-3}	density of blood [24]
	ω_b	1.1×10^{-3}	s^{-1}	normothermic hand blood flow rate [23]
	A_b	$c_b\rho_b\omega_b$	W m^{-3} °C^{-1}	coefficient from Pennes equation [1]
Semi-Empirical	u_0	34	°C	approximate mean skin temperature [23]
	v_0	37	°C	normothermic deep body temperature [23]
	f	0	W m^{-3}	hands produce little internal heat [23]
	g	700	W m^{-3}	maximal shivering metabolic heat generation rate [25]
	a_{air}	136	W m^{-2} °C^{-1}	energy dissipation coefficient from [23]
	u_{air}	−40	°C	external temp. where exposed skin freezes in seconds [30]
Ad Hoc	u_1	10	°C	little or no local blood flow for $u < 10$ °C skin temp. [30]
	u_2	32	°C	presumed normothermic local blood flow for $u > 32$ °C
	v_1	28	°C	presumed cessation of extremity blood flow for $v < 28$ °C
	v_2	37	°C	presumed normothermic extremity blood flow for $v = 37$ °C
	a_{wrist}	100	W m^{-2} °C^{-1}	ad hoc, see Section 6.4
	B_b	$0.07\,A_b$	W m^{-3} °C^{-1}	ad hoc, see Section 6.5

Cases (R2) and (R3), in which control of energy exchange involves u, perform similarly in terms of $v(t)$, $\langle u(t)\rangle_\Omega$, and $\phi_{\text{FB}}(t)$. For both cases (R2) and (R3), $v(t) \to v_0$ after a brief drop away from this temperature. However, the two cases are not identical; for example, the minimum value of $v(t)$ is 35.9 °C for case (R2) and 35.7 °C for (R3).

By contrast, case (R1) displays a quite different behavior with $v(t) \to v_L$ asymptotically. This phenomenon is explained as follows: In (R1), energy exchange is controlled by v alone, and so energy continues to flow from the core to the extremity even as $\langle u(t)\rangle_\Omega$ drops, causing $v(t)$ to decrease in turn, until $v(t)$ drops low enough to stop energy exchange. These results are shown in Figure 8.

5.1.7. Comparison of (R3) and (S3)

We now set $r(u, v)$ and $s(\langle u\rangle_\Omega, v)$ as in either (R3) or (S3). In order to demonstrate that (S3) performs similarly to (R3), we choose $\hat{u} = \hat{u}_1$ to minimize the functional

$$J(\xi) := \int_{\mathbb{R}} \left[\sigma_{\text{ramp}}(u_L, u_R; u) - \sigma_{\text{smooth}}(\xi, u_0; u)\right]^2 du, \tag{5.3}$$

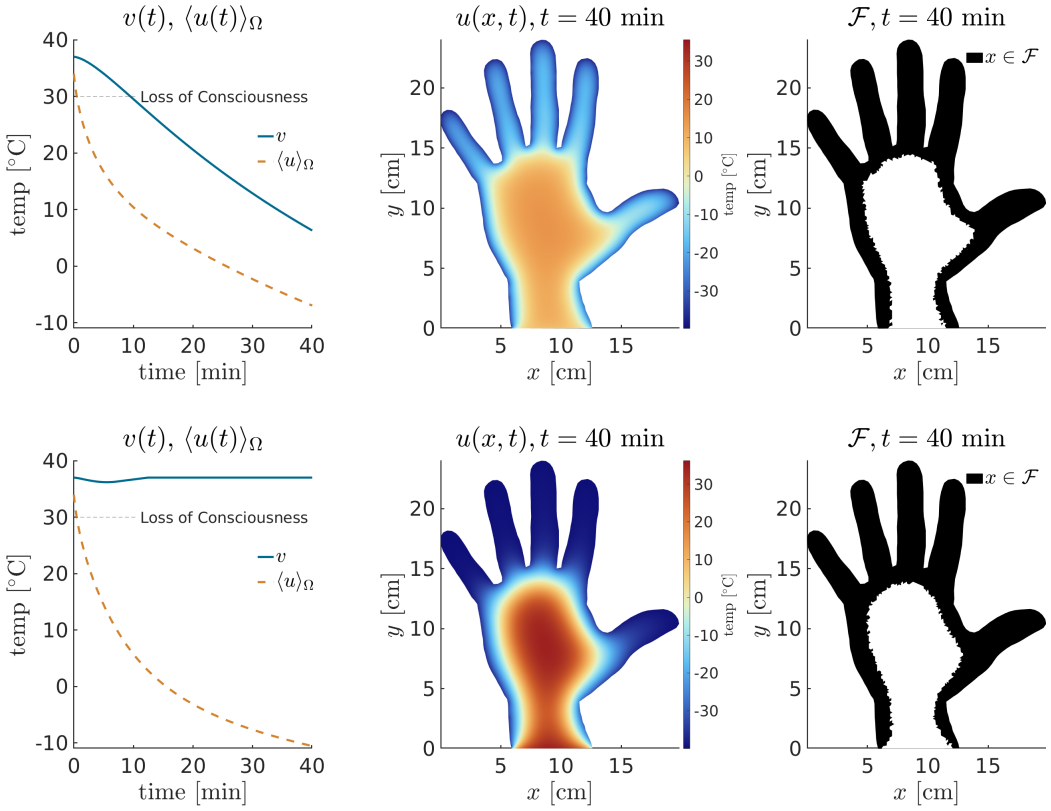

Figure 7. Comparison of simulation results for cases (C) and (R3) for the example in Section 5.1.5. Shown are a plot of $v(t)$ and $\langle u(t)\rangle_\Omega$ (left), $u(x,t)$ at $t = T$ (middle), and $\mathcal{F}$ at $t = T$ (right).

where u_L, u_R are given in Table 7 and $u_0 := \frac{1}{2}(u_L + u_R)$ ensures that σ_{ramp} and σ_{smooth} have the same half-maximum point, i.e., that $\sigma_{\text{ramp}}(u_L, u_R; u^*) = \frac{1}{2}$ and $\sigma_{\text{smooth}}(\hat{u}, u_0; u^*) = \frac{1}{2}$ for the same u^*. We choose $\hat{v} = \hat{v}_1$ and v_0 similarly. We call these choices (S3_{fit}). We also choose $\hat{u}_2 = 4\,\hat{u}_1$ and $\hat{v}_2 := 4\,\hat{v}_1$, which we call ($\text{S3}_{\text{steep}}$). These choices are summarized in Table 8. See Figure 5 for illustration. All other parameters are chosen as in Table 7.

The plots of $\langle u(t)\rangle_\Omega$ and $\phi_{\text{FB}}(t)$ are indistinguishable for (R3), (S3_{fit}), and (S3_{steep}). However, while the plots of $v(t)$ for these cases exhibit the same trend, $v(t) \to v_0$ fastest for (S3_{steep}) and slowest for (S3_{fit}). See Figure 9. These results suggest that, as expected, the specific choice of σ has an influence on the solutions of the model.

5.2. Comparison to physiological data

We now compare the simulation results of our model results to the experimental data presented in [20, 41]. In the experiments reported in these papers, test subjects sat in a 0.5 ± 0.5 °C environment for 120 min while wearing heavy, insulating clothing on their entire body (including face and head), but with their hands exposed. This condition closely matches the scenario our model is meant to simulate. Temperature sensors were placed at various locations on the subjects' bodies, including a sensor on the back of the hand and on the ring finger. Body core temperature was also recorded.

For our simulations, we set $u_{\text{init}} = 34$ °C, $v_{\text{init}} = 37$ °C, and $g = 350$ W / m^3, which is consistent

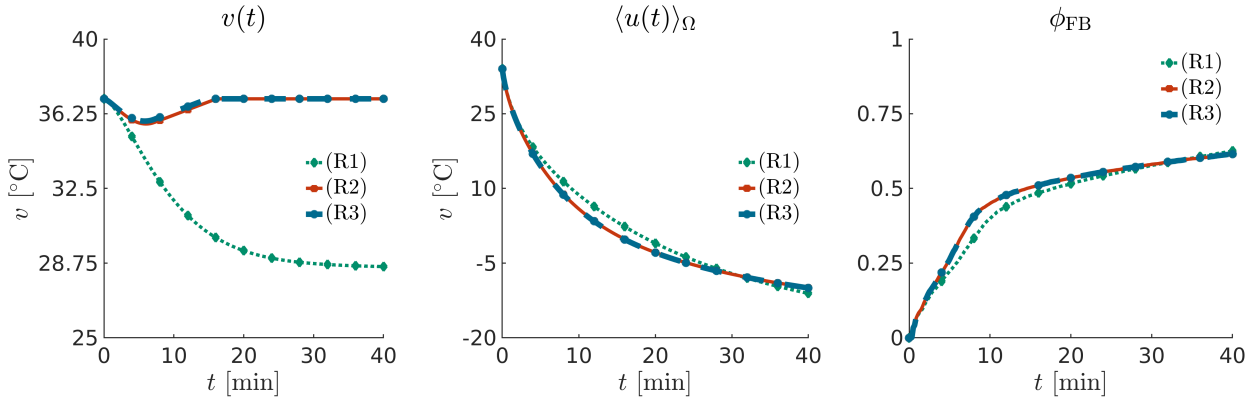

Figure 8. Comparison of simulation results for cases (R1), (R2), and (R3) for the example in Section 5.1.6. Shown are $v(t)$ (left), $\langle u(t)\rangle_\Omega$ (middle), and $\phi_{\mathrm{FB}}(t)$ (right).

Table 8. Parameters chosen to specify cases ($\mathrm{S3}_{\mathrm{fit}}$) and ($\mathrm{S3}_{\mathrm{steep}}$). The value $\hat{v}_1$ minimizes functional (5.3), for v_L, v_R as in Table 7 and $v_0 := \frac{1}{2}(v_L + v_R)$. The value $\hat{v}_2 := 4\hat{v}_1$. The values $\hat{u}_1$, $\hat{u}_2$, and u_0 are chosen similarly.

parameter	($\mathrm{S3}_{\mathrm{fit}}$)	($\mathrm{S3}_{\mathrm{steep}}$)
$\hat{v}$	$\hat{v}_1 = 0.58901$	$\hat{v}_2 = 2.3561$
$\hat{u}$	$\hat{u}_1 = 0.24096$	$\hat{u}_2 = 0.96384$
v_0	32.5	32.5
u_0	21.0	21.0

with moderate shivering at rest; see Table 4. We use boundary and initial conditions, mesh (including h), and τ as described in Section 5.1.1. We set $r(\cdot)$ and $s(\cdot)$ according to either (R3) or (SHC). All other coefficients are as in Table 7. Lastly, we let $u_{\mathrm{air}} = 0.5$ °C and $T = 120$ min ($N_T = 7200$).

In Figure 10, we report $v(t)$ as well as $\langle u\rangle_{\Omega_{\mathrm{hand}}}$ and $\langle u\rangle_{\Omega_{\mathrm{fingers}}}$ where $\Omega_{\mathrm{fingers}}$ is the portion of Ω corresponding to the fingers and $\Omega_{\mathrm{hand}} = \Omega \setminus \Omega_{\mathrm{fingers}}$. Within Ω_{core}, both (R3) and (SHC) maintain $v(t)$ within the reported physiological ranges.

Within Ω_{hand}, both (R3) and (SHC) overestimate $\langle u(t)\rangle_{\Omega_{\mathrm{hand}}}$ relative to reported physiological ranges. This may be in part due to the decision to average the temperature across this region, which includes temperatures near the wrist, which is maintained near 34 °C throughout the simulation due to the boundary condition on $\partial\Omega_{\mathrm{wrist}}$.

Lastly, within $\Omega_{\mathrm{fingers}}$, model (SHC) maintains $\langle u(t)\rangle_{\Omega_{\mathrm{fingers}}}$ at temperatures significantly closer to the reported physiological ranges than does model (R3), which consistently underestimates temperatures from about $t = 10$ min onward.

6. Sensitivity of the model

In this section, we illustrate the sensitivity to different data of the model (4.1), (4.2) with $r(\cdot)$ and $s(\cdot)$ given either by cases (C) or (R3) and boundary condition (4.3). Except when indicated, we use initial and boundary conditions and discretization as given in Section 5 and use parameters as given in Table 7. We enforce that $v \le v^* := 37$ °C; see Section 5.1.3.

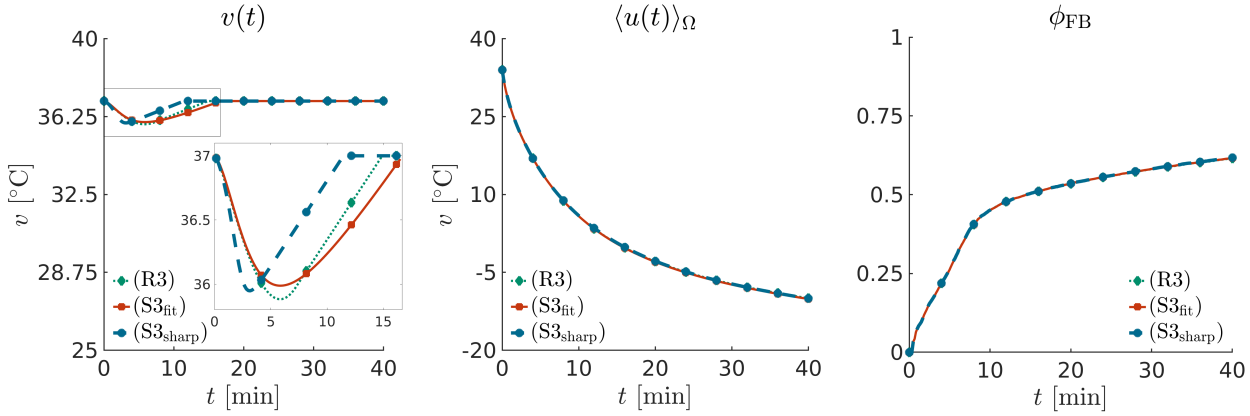

Figure 9. Comparison of simulation results for cases (R3), ($S3_{\mathrm{fit}}$), and ($S3_{\mathrm{steep}}$) for the example in Section 5.1.7: plots of $v(t)$ (left), $\langle u(t)\rangle_\Omega$ (middle), and $\phi_{\mathrm{FB}}(t)$ (right).

We often observe

$$\lim_{t\to\infty}(\langle u(t)\rangle_\Omega, v(t)) = (u_{\mathrm{cold}}, v_{\mathrm{cold}}) \tag{6.1}$$

where, despite the tendency of the exterior boundary temperature u_{air} to draw both $\langle u\rangle_\Omega$ and v down to u_{air}, the persistent source term g injects enough heat that the eventual state lies strictly above u_{air}:

$$u_{\mathrm{air}} < u_{\mathrm{cold}} < 0, \quad u_{\mathrm{air}} < v_{\mathrm{cold}} < 0.$$

The actual value of u_{cold}, v_{cold} depends on the particular choice of parameters and initial data in each experiment; our aim in this section is to study the trend exhibited on the way toward equilibrium, rather than any specific equilibrium value. Hence, we do not specify $(u_{\mathrm{cold}}, v_{\mathrm{cold}})$ and simply regard this pair as a "cold-state" equilibrium induced by the source g. Note also that (6.1) is only a hypothetical equilibrium since the model becomes irrelevant once $v(t) < 28$ °C in real world applications.

6.1. Different domains Ω

In this section, we study the dependence of the results on the particular hand geometry. We obtain photographs of four hands of various sizes and process each to be used as domain Ω. We refer to these as (G1) through (G4), numbered from smallest to largest total area; see Figure 11 for illustration and Table 9 for details. For each case, we use model (R3) for $r(\cdot)$ and $s(\cdot)$ as well as parameters from Table 7.

In these simulations, the smaller domains (G1) and (G2) were associated with lower $\langle u(t)\rangle_\Omega$ and higher $\phi_{\mathrm{FB}}(t)$ but also with higher $v(t)$ at each t. The larger domains (G3) and (G4) showed the opposite trend. This suggests that domain size does influence model performance. However, the highest $\langle u(t)\rangle_\Omega$ and lowest $v(t)$ were actually associated with geometry (G3), not (G4), suggesting that domain shape may also matter. These results are shown in Figure 12.

6.2. Varying initial conditions

We either fix u_{init} and vary v_{init} or vice versa. Specifically, we fix $u_{\mathrm{init}} = 35$ and test with $v_{\mathrm{init}} \in \{5, 10, 15, 20, 25, 30, 35\}$. We also consider $u_{\mathrm{init}} \in \{5, 10, 15, 20, 25, 30, 35\}$ and $v_{\mathrm{init}} = 5$. With these initial conditions, we simulate the model (4.1), (4.2).

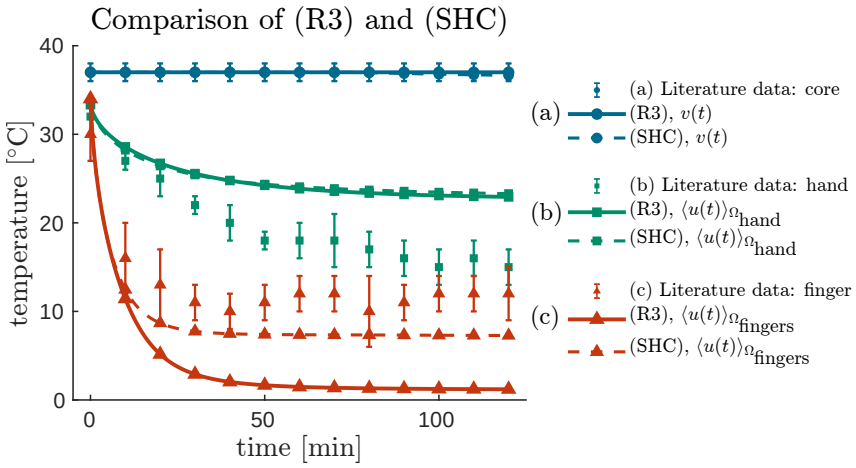

Figure 10. Comparison of models (R3) and (SHC) with data from literature for the scenario in Section 5.2. Error bars indicate ranges of experimentally obtained data, transcribed manually from [20, Figures 5 and 6]. Shown are (a) $v(t)$ and data from the sensor in the body core (top group, in blue); (b) $\langle u(t)\rangle_{\text{hand}}$ and data from the sensor on the back of the hand (middle group; in green); (c) $\langle u(t)\rangle_{\text{fingers}}$ and data from the sensor on the finger (bottom group, in red).

Table 9. Geometry data for (G1) through (G4).

	height cm	width cm
(G1)	17	10.5
(G2)	19	14.5
(G3)	22	15.5
(G4)	24	20

For all choices of $(u_{\text{init}}, v_{\text{init}})$, we observe $(\langle u\rangle_\Omega, v) \to (u_{\text{cold}}, v_{\text{cold}})$ for case (C) and $(\langle u\rangle_\Omega, v) \to (u_{\text{cold}}, v^*)$ for case (R3). Figure 13 shows these results.

6.3. Varying metabolic rate

We test the seven cases corresponding to $g = \{200n : n \in \mathbb{N} \text{ and } 0 \le n \le 6\}$. These values represent the entire range of physiologically realistic values of g; see Table 4.

For case (C), $(\langle u\rangle_\Omega, v) \to (u_{\text{cold}}, v_{\text{cold}})$, independent of the choice of g. Without the ability to regulate core-extremity exchange, energy flows from body to hand to environment at a rate greater than can be replaced by g for any of the tested values of g.

In case (R2), when $g > 0$, $(\langle u\rangle_\Omega, v) \to (u_{\text{cold}}, v^*)$. We observe an initial drop in $v(t)$, triggering a reduction of core-extremity exchange, allowing $v(t) \to v^*$ due to g. But $v(t)$ reaches a lower minimum and takes longer to recover when g is smaller. When $g = 0$, $(\langle u\rangle_\Omega, v) \to (u_{\text{cold}}, v_{\text{eq}})$, $v_{\text{eq}} \approx 34.9$ °C. Here, the core-extremity exchange is shut off and there is no heat input. So $v(t)$ neither recovers toward v^* nor drops all the way to v_{cold}.

Figure 14 shows these results; note that the vertical axes on the left and right are not set to the same scale.

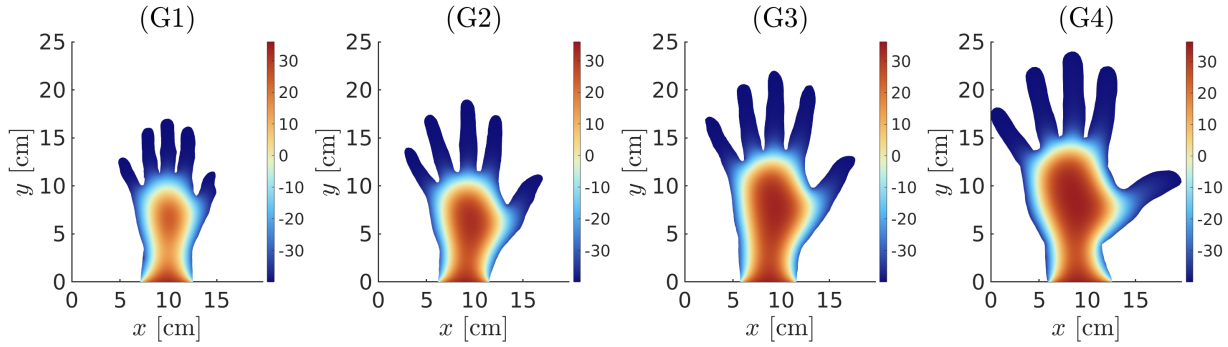

Figure 11. Plots of $u(x, T)$ for geometries (G1) through (G4) in Section 6.1.

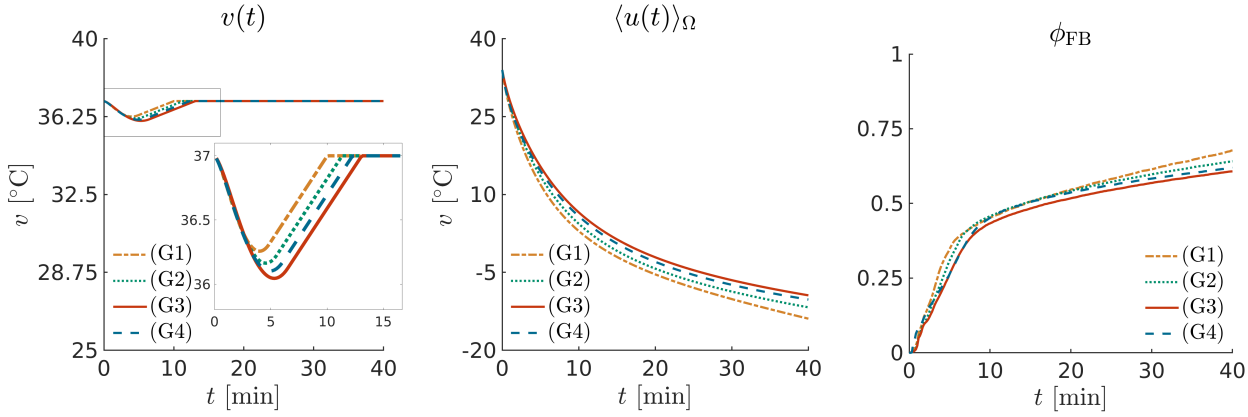

Figure 12. Plots of $v(t)$ (left), $\langle u(t)\rangle_\Omega$ (middle), and $\phi_{\text{FB}}(t)$ (right) comparing simulations on geometries (G1) through (G4) for the example in Section 6.1. The cutaway zooms in on the region of interest, expanding the v-axis to highlight local behavior.

6.4. Varying a_{wrist}

To specify the boundary conditions when $\partial\Omega_{\text{wrist}} \neq \varnothing$, we must specify a_{wrist}. However, to our knowledge, an appropriate range for a_{wrist} does not exist in the literature; the choice is at present ad hoc. Here, we demonstrate that the model is not very sensitive to the choice of a_{wrist}.

We set the coefficient a_{wrist} to be one of $\{0, 10, 10^2, 10^3, 10^4, 10^5, 10^6\}$ and plot the corresponding results in Figure 15. We observe that, although a_{wrist} has a strong local influence on $u(x, t)$ near $\partial\Omega_{\text{wrist}}$, it appears to have almost no influence on the dynamics between v and $\langle u\rangle_\Omega$ as shown in Figure 16; note that the vertical axes on the left and right are not set to the same scale.

6.5. Varying B_b

To specify model (4.1), (4.2) with $r(\cdot)$ and $s(\cdot)$ given by any choice of (C), (R1) through (R3), or (S1) through (S3), we must choose B_b, which determines the strength of the coupling in (4.2). As in Section 6.4, this choice is ad hoc. Here, we demonstrate that the performance of the model is sensitive to the choice of B_b.

We let $B_b = \mu A_b$ where $\mu \in \{2n/5 : n \in \mathbb{N} \text{ and } 0 \leq n \leq 5\}$.

For case (C), $(\langle u\rangle_\Omega, v) \to (u_{\text{cold}}, v_{\text{cold}})$ as $t \to \infty$ for any $B_b > 0$. Note though that when $B = 0$, $v = v^*$ throughout the simulation, as (4.2) no longer depends on $\langle u\rangle_\Omega$.

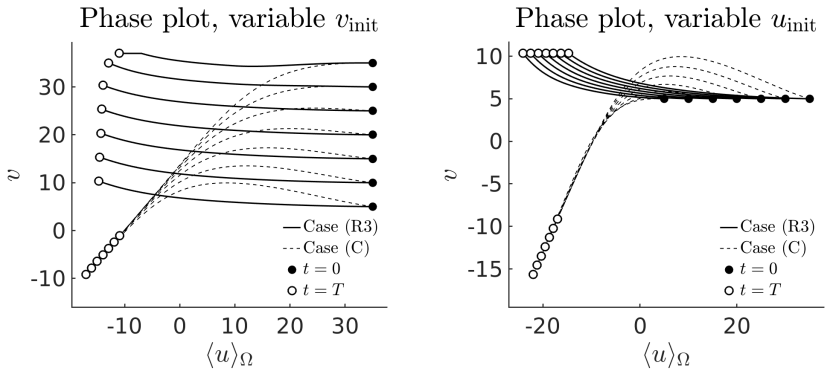

Figure 13. Phase plot of v against $\langle u \rangle_\Omega$ illustrating sensitivity to initial conditions in the example in Section 6.2. (Left) Trajectories starting from $u_{\text{init}} = 35$ and $v_{\text{init}} = \{5, 10, 15, 20, 25, 30, 35\}$. (Right) Trajectories starting from $u_{\text{init}} = \{5, 10, 15, 20, 25, 30, 35\}$ and $v_{\text{init}} = 5$.

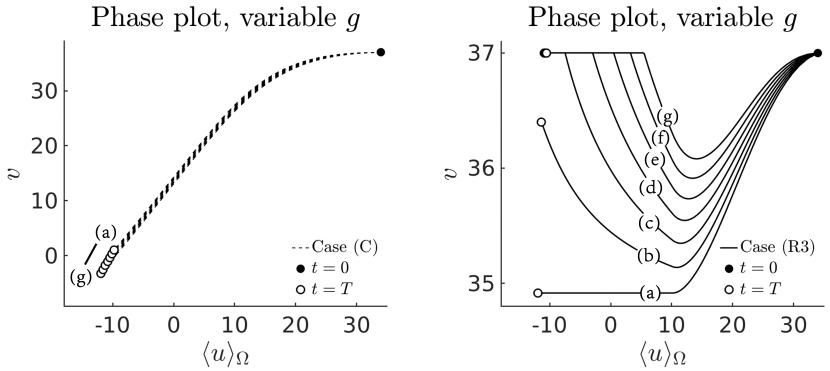

Figure 14. Phase plot of v against $\langle u \rangle_\Omega$ illustrating sensitivity to g for the example in Section 6.3. Markers (a) through (g) correspond to the values $g = 0$ through $g = 1200$. (Left) Trajectories for case (C). (Right) Trajectories for case (R3).

For case (R2), we see $(\langle u \rangle_\Omega, v) \to (u_{\text{cold}}, v^*)$, with a drop in $v(t)$ leading to a reduction of core-extremity exchange, and a subsequent recovery of $v \to v^*$. But the trajectories show significant sensitivity to B_b, with lower minima and longer recovery times associated with greater values of B_b.

Figure 17 presents these results. It is interesting to note that, physiologically, the difference between a small and large value of B_b corresponds to the difference between an unpleasant experience and a life-threatening one.

7. Summary and conclusion

In this paper, we presented a new coupled PDE-ODE bioheat model for simulating the thermoregulatory interaction between core body temperature and extremity temperature during cold exposure, with specific application to hypothermia and frostbite. The PDE describes transient heat conduction in an extremity, while the ODE models spatially averaged core temperature. The model incorporates nonlinear, physiologically motivated coupling terms representing local and reflex vasoconstriction, as well as environmental heat exchange.

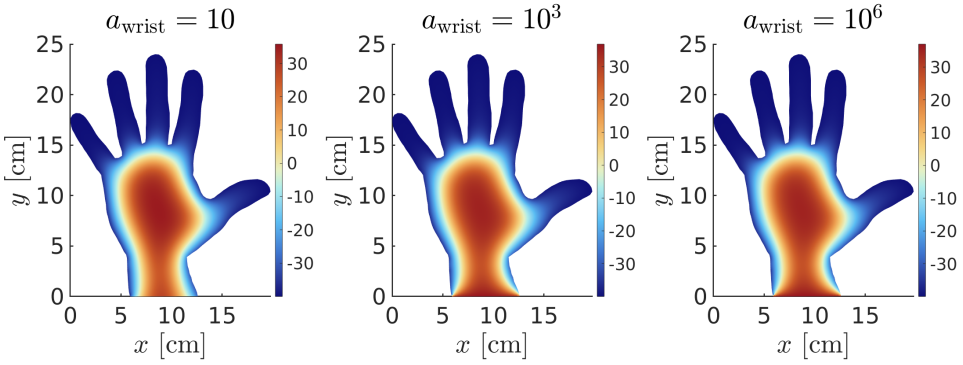

Figure 15. Plot of $u(x,t)$ in Ω at $t = T$ for $a_{\text{wrist}} = 10$ (left), $a_{\text{wrist}} = 10^3$ (center), and $a_{\text{wrist}} = 10^6$ (right) for the example in Section 6.4.

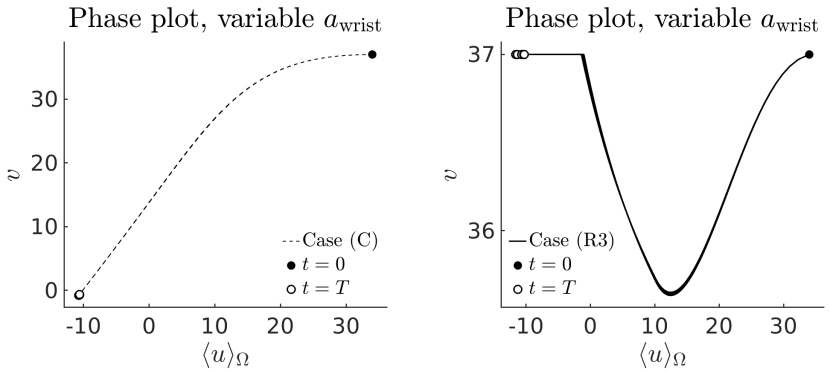

Figure 16. Phase plot of v against $\langle u \rangle_\Omega$ illustrating insensitivity to a_{wrist} for the example in Section 6.4. Trajectories for the values $a_{\text{wrist}} = 0$ through $a_{\text{wrist}} = 10^6$ are plotted, but no attempt has been made to label individual curves, as these curves are too close to disambiguate, despite orders of magnitude difference in a_{wrist}. (Left) Trajectories for case (C). (Right) Trajectories for case (R3).

Our numerical results illustrated the model's ability to reproduce physiologically realistic scenarios. We compared different coupling laws (constant, ramp, smooth, SHC) which, in particular, demonstrated the need for nonlinear coupling to obtain physiologically realistic simulations. We also conducted sensitivity studies to explore the impact of geometric variation, initial conditions, metabolic heat production, and coupling/boundary parameters. These studies showed that while some ad hoc parameters (e.g., a_{wrist} in (4.3)) have minimal influence, others (e.g., B_b in (C), (R1) through (R3), and (S1) through (S3)) can dramatically alter outcomes.

The proposed framework thus provides a physiologically relevant tool for studying cold-induced injuries. We also see potential for extensions.

First, our model could be extended to include more than one compartment and extremity.

Second, in our simulations, we restricted attention to relatively simple forms of the nonlinear coupling and to linear (Robin) boundary conditions. But the model could be further developed to account for additional physiological details and to include radiation boundary conditions.

Third, the parameter B_b is at present entirely ad hoc. Given the sensitivity to this parameter that we have demonstrated in Section 6.5, further study is warranted.

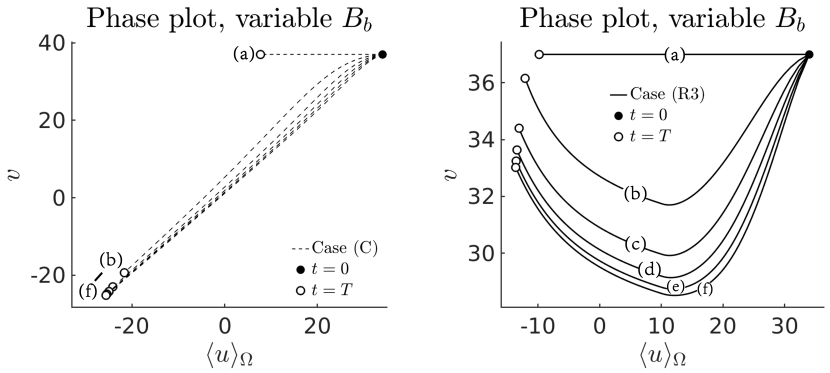

Figure 17. Phase plot of v against $\langle u \rangle_\Omega$ illustrating their sensitivity to B_b in the example in Section 6.5. Left: trajectories for case (C). Right: trajectories for case (R3). Markers (a) through (f) correspond to the values $B_b = 0$ through $B_b = 2A_b$.

Finally, we note that in a forthcoming paper [21], under certain reasonable assumptions on the data and coefficients, we prove a stability estimate for this model and also for a P1 Lagrange finite element discretization of the model with backward Euler time stepping. We also prove an *a priori* error estimate for the discrete model, and provide numerical validation of the *a priori* estimate. We note that all of the choices of $r(\cdot)$, $s(\cdot)$, and $\alpha(\cdot)$ in the current paper meet the assumptions used in these proofs in [21]. Thus, our model is both physiologically relevant and mathematically rigorous.

Use of AI tools declaration

The authors declare they have not used Artificial Intelligence (AI) tools in the creation of this article.

Acknowledgments

This research was partially supported by the grants NSF DMS-2309682, DMS-1912938 under principal investigator Malgorzata Peszynska of Oregon State University. We also acknowledge the support from Joel Davis Scholar fund, awarded to Malgorzata Peszynska, Oregon State University. We wish also to thank the anonymous referees who made us aware of additional literature and whose remarks helped us to improve the paper.

Conflict of interest

The authors declare there is no conflict of interest.

References

1. H. H. Pennes, Analysis of tissue and arterial blood temperatures in the resting human forearm, *J. Appl. Physiol.*, **1** (1948), 93–122. https://doi.org/10.1152/jappl.1998.85.1.5
2. H. Klinger, Heat transfer in perfused biological tissue—I: General theory, *Bull. Math. Biol.*, **36** (1974), 403–415. https://doi.org/10.1007/bf02464617

3. W. Wulff, The energy conservation equation for living tissue, *IEEE Trans. Biomed. Eng.*, **6** (2007), 494–495. https://doi.org/10.1109/tbme.1974.324342
4. M. M. Chen, K. R. Holmes, Microvascular contributions in tissue heat transfer, *Ann. N. Y. Acad. Sci.*, **335** (1980), 137–150. https://doi.org/10.1111/j.1749-6632.1980.tb50742.x
5. P. Deuflhard, R. Hochmuth, Multiscale analysis of thermoregulation in the human microvascular system, *Math. Method Appl. Sci.*, **27** (2004), 971–989. https://doi.org/10.1002/mma.499
6. C. Timofte, Homogenization results for dynamical heat transfer problems in heterogeneous biological tissues, *Bull. Transilv. Univ. Brasov, Ser. III, Math. Comput. Sci.*, **2** (2009), 143–148.
7. C. D'angelo, A. Quarteroni, On the coupling of 1d and 3d diffusion-reaction equations: Application to tissue perfusion problems, *Math. Models Methods Appl. Sci.*, **18** (2008), 1481–1504. https://doi.org/10.1142/s0218202508003108
8. I. G. Gjerde, K. Kumar, J. M. Nordbotten, A mixed approach to the Poisson problem with line sources, *SIAM J. Numer. Anal.*, **59** (2021), 1117–1139. https://doi.org/10.1137/19m1296549
9. Z.-Z. He, J. Liu, A coupled continuum-discrete bioheat transfer model for vascularized tissue, *Int. J. Heat Mass Transf.*, **107** (2017), 544–556. https://doi.org/10.1016/j.ijheatmasstransfer.2016.11.053
10. D. Notaro, L. Cattaneo, L. Formaggia, A. Scotti, P. Zunino, A mixed finite element method for modeling the fluid exchange between microcirculation and tissue interstitium, in *Advances in Discretization Methods: Discontinuities, Virtual Elements, Fictitious Domain Methods*, **12** (2016) 3–25. https://doi.org/10.1007/978-3-319-41246-7_1
11. G. I. Barenblatt, I. P. Zheltov, I. N. Kochina, Basic concepts in the theory of seepage of homogeneous liquids in fissured rocks (strata), *J. Appl. Math. Mech.*, **24** (1960), 1286–1303. https://doi.org/10.1016/0021-8928(60)90107-6
12. R. E. Showalter, D. B. Visarraga, Double-diffusion models from a highly-heterogeneous medium, *J. Math. Anal. Appl.*, **295** (2004), 191–210.
13. V. Klein, M. Peszynska, Adaptive double-diffusion model and comparison to a highly heterogenous micro-model, *J. Appl. Math.*, **2012** (2012). https://doi.org/10.1016/s0022-247x(04)00244-6
14. M. Peszynska, T. Fara, M. Phelps, N. Zhang, Mixed dimensional modeling with overlapping continua on Cartesian grids for complex applications, in *Finite Volumes for Complex Applications X—Volume 1, Elliptic and Parabolic Problems* **432** (2023), 129–145. https://doi.org/10.1007/978-3-031-40864-9_8
15. E. Majchrzak, B. Mochnacki, M. Dziewoński, M. Jasiński, Numerical modeling of hyperthermia and hypothermia processes, *Adv. Mater. Res.*, **268** (2011), 257–262. https://doi.org/10.4028/www.scientific.net/amr.268-270.257
16. J. Chiang, P. Wang, C. L. Brace, Computational modelling of microwave tumour ablations, *Int. J. Hyperth.*, **29** (2013), 308–317. https://doi.org/10.3109/02656736.2013.799295
17. J. A. Stolwijk, *A mathematical model of physiological temperature regulation in man*, Technical report, NASA, 1971.
18. J. A. Stolwijk, J. D. Hardy, Control of body temperature, *Compr. Physiol.*, (1977), 45–68. https://doi.org/10.1002/cphy.cp090104

19. X. Xu, T. P. Rioux, M. P. Castellani, Three dimensional models of human thermoregulation: A review, *J. Therm. Biol.*, **112** (2023). https://doi.org/10.1016/j.jtherbio.2023.103491

20. M. P. Castellani, T. P. Rioux, J. W. Castellani, A. W. Potter, X. Xu, A geometrically accurate 3 dimensional model of human thermoregulation for transient cold and hot environments, *Comput. Biol. Med.*, **138** (2021). https://doi.org/10.1016/j.compbiomed.2021.104892

21. T. Fara, M. Peszynska, Nonlinear bioheat model for dynamics of hypothermia and frostbite. II. Stability analysis and finite element discretization. (2025) Manuscript in preparation.

22. K. Atkinson, W. Han, *Theoretical Numerical Analysis*, 3^{rd} edition, Springer, Dordrecht, 2009. https://doi.org/10.1007/978-0-387-28769-0

23. N. A. Taylor, C. A. Machado-Moreira, A. M. van den Heuvel, J. N. Caldwell, Hands and feet: Physiological insulators, radiators and evaporators, *Eur. J. Appl. Physiol.*, **114** (2014), 2037–2060. https://doi.org/10.1007/s00421-014-2940-8

24. P. Hasgall, F. Di Gennaro, C. Baumgartner, E. Neufeld, B. Lloyd, M. C. Gosselin, et al., IT'IS Database for thermal and electromagnetic parameters of biological tissues, Version 4.1, https://doi.org/10.13099/VIP21000-04-1

25. W. F. Boron, E. L. Boulpaep, *Medical Physiology*, 2^{nd} edition, Elsevier Health Sciences, 2012.

26. A. Bensoussan, J. L. Lions, G. Papanicolaou, *Asymptotic Analysis for Periodic Structures*, North-Holland Publishing Co., Amsterdam, 1978.

27. J. E. Hall, M. E. Hall, *Guyton and Hall Textbook of Medical Physiology E-Book*, Elsevier Health Sciences, 2020.

28. M. Peszynska, R. E. Showalter, Multiscale elliptic-parabolic systems for flow and transport, *Electr. J. Differ. Equ.*, **2007** (2007).

29. P. Orlowski, F. K. McConnell, S. Payne, A mathematical model of cellular metabolism during ischemic stroke and hypothermia, *IEEE Trans. Biomed. Eng.*, **61** (2013), 484–490. https://doi.org/10.1109/tbme.2013.2282603

30. K. Collins, *Hypothermia: The Facts*, Oxford University Press, 1983.

31. J. W. Castellani, A. J. Young, Human physiological responses to cold exposure: Acute responses and acclimatization to prolonged exposure, *Auton. Neurosci.*, **196** (2016), 63–74. https://doi.org/10.1016/j.autneu.2016.02.009

32. M. N. Cramer, D. Gagnon, O. Laitano, C. G. Crandall, Human temperature regulation under heat stress in health, disease, and injury, *Physiol. Rev.*, **102** (2022), 1907–1989. https://doi.org/10.1152/physrev.00047.2021

33. N. Charkoudian, Skin blood flow in adult human thermoregulation: how it works, when it does not, and why, in *Mayo Clin. Proc.*, **78** (2003), 603–612. https://doi.org/10.4065/78.5.603

34. H. T. Meryman, Tissue freezing and local cold injury, *Physiol. Rev.*, **37** (1957), 233–251. https://doi.org/10.1152/physrev.1957.37.2.233

35. B. K. Alba, J. W. Castellani, N. Charkoudian, Cold-induced cutaneous vasoconstriction in humans: Function, dysfunction and the distinctly counterproductive, *Exp. Physiol.*, **104** (2019), 1202–1214. https://doi.org/10.1113/ep087718

36. A. Alhammali, M. Peszynska, C. Shin, Numerical analysis of a mixed finite element approximation of a coupled system modeling biofilm growth in porous media with simulations, *Int. J. Numer. Anal. Model.*, **21** (2024), 20–64. https://doi.org/10.4208/ijnam2024-1002

37. C. Shin, A. Alhammali, L. Bigler, N. Vohra, M. Peszynska, Coupled flow and biomass-nutrient growth at pore-scale with permeable biofilm, adaptive singularity and multiple species, *Math. Biosci. Eng.*, **18** (2021), 2097–2149, https://doi.org/10.3934/mbe.2021108

38. A. J. Q. Alfaro, I. J. R. Acosta, J. D. Cardona, A. F. H. Ortiz, J. D. C. Ortegón, Severe frostbite due to extreme altitude climbing in South America: A case report, *Cureus*, **14** (2022). https://doi.org/10.7759/cureus.27771

39. P. Jud, F. Hafner, M. Brodmann, Frostbite of the hands after paragliding: A chilling experience, *The Lancet*, **394** (2019), 2282. https://doi.org/10.1016/s0140-6736(19)32960-5

40. D. M.-A. Magnan, M. Gelsomino, P. Louge, R. Pignel, Successful delayed hyperbaric oxygen therapy and iloprost treatment on severe frostbite at high altitude, *High Alt. Med. Biol.*, **23** (2022), 294–297. https://doi.org/10.1089/ham.2021.0172

41. J. W. Castellani, B. R. Yurkevicius, M. L. Jones, T. J. Driscoll, C. M. Cowell, L. Smith, et al., Effect of localized microclimate heating on peripheral skin temperatures and manual dexterity during cold exposure, *J. Appl. Physiol.*, **125** (2018), 1498–1510. https://doi.org/10.1152/japplphysiol.00513.2018

AIMS Press